The Thesis Committee for Thomas Harland Hundley
Certifies that this is the approved version of the following thesis:

Size Distribution and Spatial Arrangement of Normal Faults in A-Bomb Canyon, Buckskin Mountains, Western Arizona

APPROVED BY
SUPERVISING COMMITTEE:

Supervisor:

Randall Marrett

Mark A. Helper

Mark Cloos

Size Distribution and Spatial Arrangement of Normal Faults in A-Bomb Canyon, Buckskin Mountains, Western Arizona

by

Thomas Harland Hundley, B.S.

Thesis

Presented to the Faculty of the Graduate School of

The University of Texas at Austin

in Partial Fulfillment

of the Requirements

for the Degree of

Master of Science in Geological Sciences

The University of Texas at Austin

May 2017

Acknowledgements

Mom and Dad, thank you for the unending support throughout my entire academic career. It hasn't always gone the way I've wanted and I wouldn't have made it through without your advice and support. Thank you for always listening and trying to offer advice to help me best persevere throughout my life.

Will and Emily, thank you for always making time to see me when I took a break from graduate school and came home. I always enjoy spending time with the two of you and the times I saw you always brightened my day. I look forward to watching Harper grow up as her fun-loving uncle and a part of your family.

Bridget, I cannot thank you enough for being an unending source of support while I completed my thesis. Whether it was listening to me when I was frustrated or coming to visit me for fun weekends to get away from graduate school I couldn't ask for anything better. I hope that I can provide the same support for you as you finish up your thesis as well.

Randy, it has been a long and fun journey full of twists and turns. You gave me the opportunity to attend the University of Texas and I will never be able to thank you enough you for that.

Steve, thank you for helping me so much at a time when I was fairly lost in the journey of graduate school. You stepped in and provided unparalleled advice and guidance that made this project possible.

Mark and Mark, Mark and Earle, thank you for your patience and for accepting the challenge of being on my committee.

Philip, what is there I can say to thank you for all of your help during my time here at the University of Texas? You are an amazing asset to all graduate students here and without you many of us wouldn't navigate graduate school so smoothly. It only took 2.5 years but I finally managed to call you Philip instead of Mr. Guerrero.

Abstract

Size Distribution and Spatial Arrangement of Normal Faults in A-Bomb Canyon, Buckskin Mountains, Western Arizona

Thomas Harland Hundley, M.S.Geo.Sci.

The University of Texas at Austin, 2017

Supervisor: Randall Marrett

The spatial arrangement of structural features, such as faults, can be randomly located, clustered together, or anti-clustered in space. The objective of this project is to understand the spatial arrangement of normal faults in A-Bomb Canyon, in the Buckskin Mountains of Arizona, as a function of fault offset, herein defined as displacement. The normalized correlation count (NCC) methodology is used in this study to quantify the spatial arrangement of faults. In the process of studying the arrangement of faults at A-Bomb Canyon, the displacement distribution, coefficient of variation as well as the NCC are examined to understand whether the faults cluster or are randomly spaced and if clustered, whether clusters show fractal scaling. Data analysis uses a traditional approach of size distribution analysis along with the correlation count technique. Results show that the frequency distribution of fault displacements follows a power law that spans ~four orders of magnitude. Faults with displacement thresholds of less than 1 meter display plateau patterns in NCC, indicate clustering at varying spacing, but clustering is not self-organized. Normal faults with > 1 meter displacement reflects faults with a dominant spacing of approximately twenty meters.

Table of Contents

List of Tables

List of Figures

Section 1. Introduction

Normal faults are the primary structures accommodating extension in the brittle part of the crust. The displacement patterns of normal faults and fracture systems have long been a topic of interest, as the scaling of fault/fracture systems is motivated by practical applications in several fields including earthquake hazard assessment and hydrocarbon reservoir management (Bonnet et al., 2001). Faults within a fault system have typically been described by scaling laws characterizing their spatial (Bour and Davy, 1999; Du Bernard et al., 2002; Gibbons, 2006) or size distribution of fault displacements (Marrett et al., 1999; Hooker et al., 2014). Past spatial arrangement studies, including statistical analyses of nearest neighbor spacings (Priest and Hudson, 1976; Narr and Suppe, 1991), were shown to have limited utility (Gomez and Marrett, in review) because the studies quantify only nearest neighbors and ignore the sequence of spacings. The methodology used in this research accounts for the sequence of spacings and complements descriptive statistics to provide a more robust understanding. Using a well-exposed example of normal faults that range over at least five orders of displacement magnitude of size (hereinafter simply "size"), this study examines fault size distribution utilizing a new method for spatial arrangement analysis, the correlation count methodology (Marrett et al., in review). Size patterns and spatial arrangement of faults are investigated using this more robust approach to quantifying spatial patterns (Marrett et al., in review).

Section 2. Tectonic Setting

The study area is located in the Buckskin-Rawhide metamorphic core complex in western Arizona. Metamorphic core complexes consist of a basement terrane and an unmetamorphosed cover separated by extensional faults or detachments. Core complexes develop by tectonic denudation, whereby a low-angle normal fault emplaces younger shallow rocks on top of deeper-level, older rocks. Progressive exhumation results in younger brittle deformation that over-prints earlier ductily deformed rock (Armstrong, 1982). Core complexes exhibit an asymmetric dome-like form and typically form high topographic areas in this region (Coney, 1980).

Covering approximately 800 square kilometers, the Buckskin-Rawhide metamorphic core complex (BRMCC) is among the largest in the Colorado River extensional corridor and is one of the classic metamorphic core complexes localities in the world (Singleton, 2012). The BRMCC region provides distinct exposure of detachment faults linked to northeast-directed, large-magnitude (kilometric) extension. Spencer and Reynolds (1991) determined that the Buckskin-Rawhide Mountains and adjacent Harquahala, Harcuvar, and Whipple Mountains comprise a sequence of corrugated footwalls that are part of the same detachment fault system. They concluded total extension across the West Central Arizona detachments is approximately 55-75 km. Extensional unroofing of the BRMCC core complex occurred primarily in the early to middle Miocene (Richard et al., 1990; Foster et al., 1993; Scott et al., 1998; Carter et al., 2004). Proterozoic and Mesozoic layered granitoids and gneisses, Paleozoic and/or Mesozoic metasedimentary rocks, and Tertiary granitoids are the primary lithologies of the mylonitic lower plate (Bryant, 1995).

A-Bomb Canyon, the location of this study, is in the Buckskin-Rawhide Mountains (Figure 1). These ranges contain the most extensive exposures of stacked Mesozoic thrust faults in Arizona and California (Laubach, 1986, Reynolds et al., 1986, and Richard et al., in press). With minor exceptions, the thrusts are southwest, south, and southeast directed (Spencer et al., 1987). Thrust faults within the core complexes demonstrably predate Tertiary extension (Spencer et al., 1987). Near A-Bomb Canyon the detachment fault is sub-horizontal (Spencer and Reynolds, 1989).

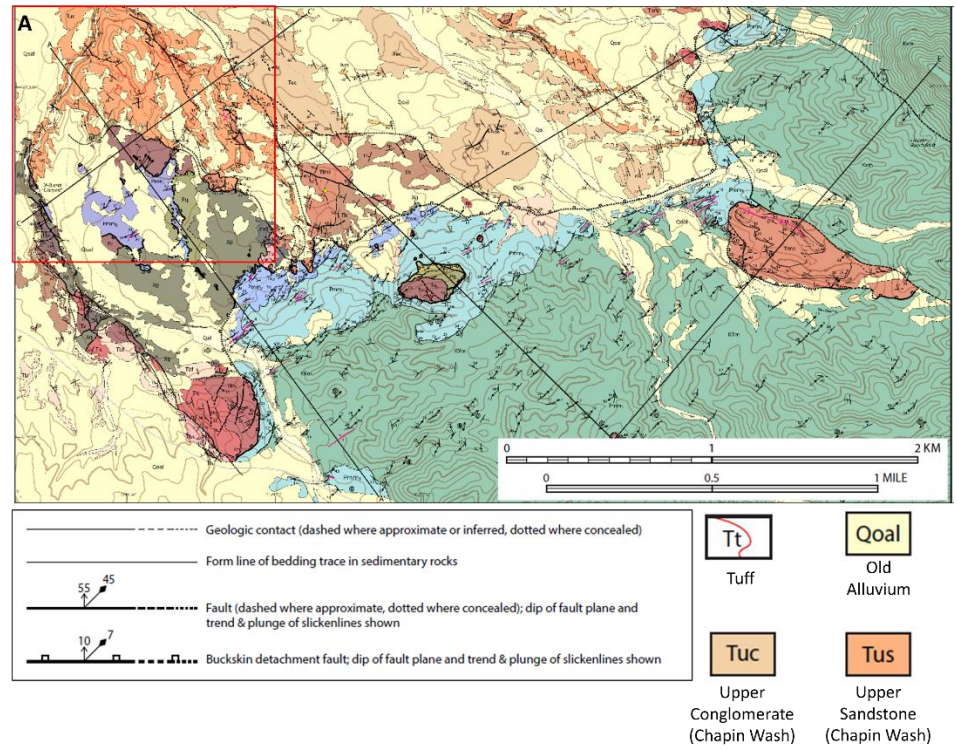

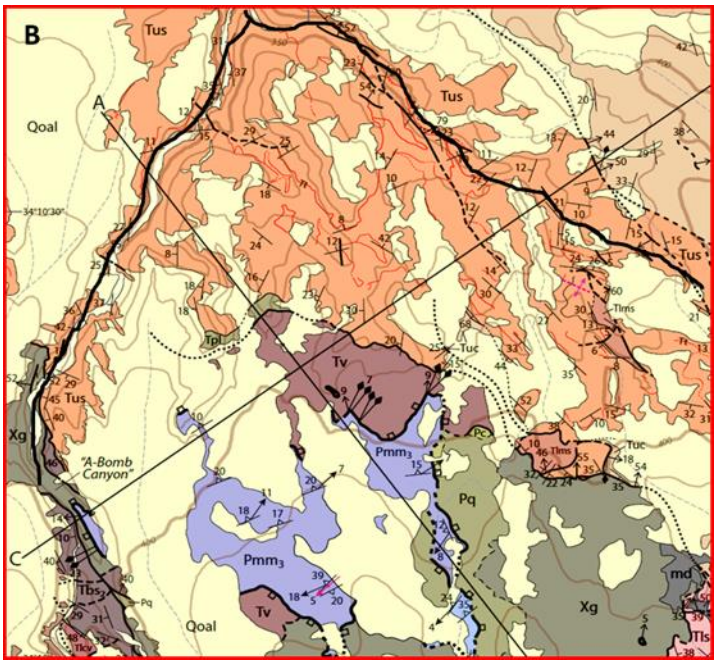

Figure 1: A) Geologic map of the Southern Lincoln Ranch Basin in West-Central Arizona. (Singleton, J., Bird, E., and Hatfield, M., 2014) B) Enlargement of the A-Bomb Canyon area of the geologic map. A-Bomb Canyon represented by the thick black line. See Figure 2 for rock unit abbreviations not contained in Figure 1A.

Section 3. Geology of A-Bomb Canyon

The focus of this research is faulted Miocene sedimentary rocks directly above mylonitic and chlorite breccia of the Buckskin-Rawhide detachment (Singleton, 2012). Upper plate rocks are well-exposed in A-Bomb Canyon (Spencer et al., 1987; Laubach et al., 1992) in the southern Lincoln Ranch Basin (LRB) of the Buckskin-Rawhide Mountains. The stratigraphy of the upper plate in A-Bomb Canyon consists of undeformed pediment conglomerate that unconformably overlies the Sandtrap Conglomerate Formation and Chapin Wash Formation (Figure 2).

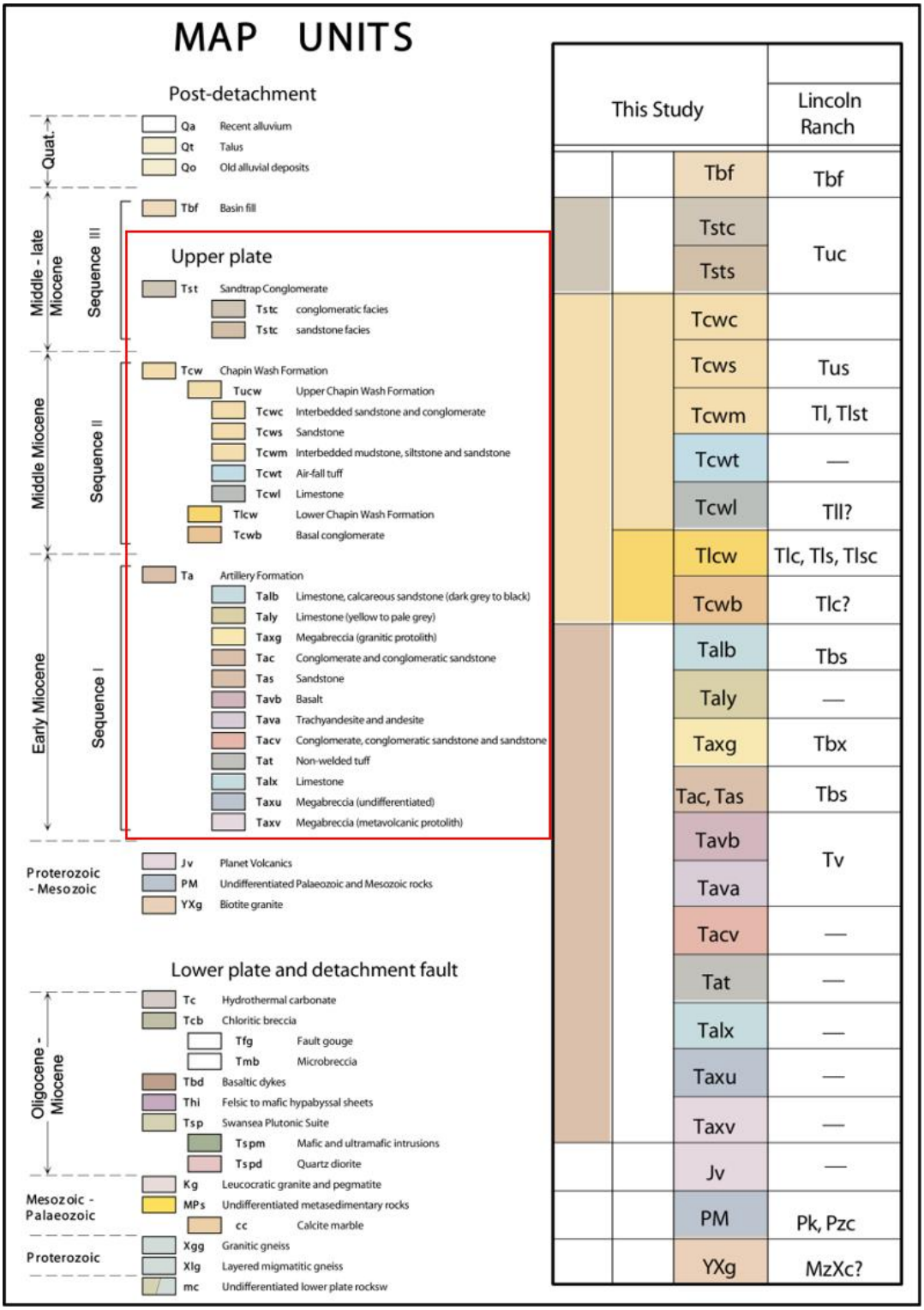

Figure 2: Stratigraphic column of the Buckskin-Rawhide Mountains, La Paz and Mohave Counties, Arizona with Lincoln Ranch specific unit abbreviations (from R.J. Scott, 2004). The geologic units encountered in this study in the upper plate (denoted by red box) are the Chapin Wash Formation and the Sandtrap Conglomerate.

STRATIGRAPHY

A-Bomb Canyon was incised through upper plate rocks down to the detachment. The canyon floor locally exposes the Buckskin-Rawhide detachment fault below which Proterozoic granitoids, characterized by a deep green coloration, starkly contrast with upper plate rocks. The sharp fault contact contains shattered granites in the upper-plate above a broken lens of dark-brown carbonate exposed at the base of the upper-plate granite (Spencer et al., 1987). Chloritic breccia and micro-breccia below the fault contain "floating" porphyroclasts of granitic and gneissic mylonite (Spencer et al., 1987). A high-angle normal fault crossing the canyon that places red Miocene sandstone (Chapin Wash Formation) down against the shattered granite was noted (Spencer et al., 1987). Field observations during the canyon traverse confirmed this fault. Lower-plate metamorphic rocks are unexposed along fault scanlines, which surveyed faults in exclusively upper-plate rocks.

Most outcrops in A-Bomb Canyon expose upper-plate strata of the Miocene Chapin Wash Formation, dominantly fine-grained red sandstones and siltstones. Sandstone beds range in thickness from centimeters to decimeters (Laubach et al., 1992), but are typically 10 cm or less thick. Siltstone beds and laminae range from 0.2 cm to 3 cm thick. Sharp contacts between sandstone and siltstone layers constrain displacement of normal faults smaller than 1 mm. Most individual sandstone and siltstone layers have stratigraphic continuity across 10+ meters laterally and are only discontinuous where offset by faults. As a consequence, layering provides useful markers for fault displacement that exceeds layer thickness. Laubach et al. (1992) reported that stratigraphic layers do not thicken across faults. They concluded that the presence of grain fracturing and gouge formation along the faults show that lithification of the unit occurred before faulting.

Distinctive beds within the otherwise monotonous Chapin Wash Formation include tuff layers and conglomeratic soles of some sandstones, which were useful for measuring faults having displacement > 1 m. In particular, a conspicuous pair of tuff layers are 15-250 cm thick, white-light gray, reworked volcanic ash intercalated with sandstone laminae (Singleton et al., 2014). Where crossed by survey lines, the tuffs are stratigraphically separated by 8 m, but farther south, the lower tuff is truncated beneath an intraformational unconformity (Figure 3). It is possible that tectonic deformation began before or during deposition of the Chapin Wash Formation, but in any case, fault displacements of Chapin Wash Formation layers cannot be

older than their depositional age. A weighted mean 206Pb/238U age constraint of approximately 14.7 ± 0.6 Ma of one of the tuff layers within the Chapin Wash Formation (Prior et al., 2016), indicates that the Chapin Wash Formation is middle Miocene. (Prior et al., 2016).

Figure 3: Field photograph of the intraformational unconformity within the Chapin Wash Formation truncating the lower tuff, here dipping to the left. Note person for scale.

The Sandtrap Conglomerate depositionally overlies the Chapin Wash Formation across the LRB (Figure 1), but in A-Bomb Canyon the two units occur in fault contact. In A-Bomb Canyon, it contains well-rounded, poorly sorted, cobble- to pebble-size clasts defining a weak bedding. The depositional base of the Sandtrap Conglomerate is unexposed where studied, but it is lithologically distinct from fine-grained sandstone and siltstones of the underlying Chapin Wash Formation.

Steep topographic walls define A-Bomb Canyon and yield the best exposures of Sandtrap Conglomerate and all older rock units. A sharp inflection point marks topography at the upper limit of canyon walls beyond which the terrain surrounding A-Bomb Canyon follows a broad,

gently NNW-sloping surface. Exposures near the trace of topographic inflection systematically reveal a 5-10 m thick pediment layer consisting of unlithified sand-pebble-cobble clasts that conspicuously include strongly lineated quartzite cobbles. Although the age of the pediment is unknown, there is no evidence of fault scarps on the upper surface of the pediment, nor is there evidence of fault displacement at its basal unconformity. Fault displacements observed in outcrops of Chapin Wash Formation and Sandtrap Conglomerate must have ceased before pediment deposition.

FAULTS

Two faults were too large to measure, their offsets being greater than 30 meters and lacking marker beds on either side for correlation across the fault. Fault offsets were measured in a plane perpendicular to the fault surface. Displacements varied from a centimeter to several tens of meters. Where observed, slickenlines were measured. Measurements confirm a rake of 90o, as previously reported by Laubach and others (1992; Figure 4).

Figure 4: Fault B (see Figure 6 for location), showing down-dip slickenlines on the well-exposed fault plane.

TIMING OF FAULTING

For this study, only the late Cenozoic tectonics of the Buckskin and Rawhide mountains is directly relevant because the faults studied cut strata deposited during the Miocene. A pulse of extensional deformation during the Oligocene to the mid Miocene created brittle and ductile structures (Spencer and Reynolds, 1989), including the Buckskin-Rawhide detachment fault. All of the faults of this study cut layering of the Chapin Wash Formation, but none of the faults cut the pediment. A whole-rock K-Ar age of 16.2±0.4 Ma for basalt from the upper Artillery Formation (Shackleford, 1980), which underlies the Chapin Wash Formation (Figure 2), places an upper age constraint on the Chapin Wash Formation. Together with the aforementioned date of 14.7 ± 0.6 Ma for one of the tuff layers within the Chapin Wash Formation, this age is consistent with faults in this study being middle Miocene or younger, indicating formation during extension along the Buckskin-Rawhide detachment.

GEOMETRY OF FAULTS

Spencer and Reynolds (1989) noted four types of Tertiary structures within the LRB area and qualitatively characterized them as 1) moderate-angle normal faults within the upper plate; 2) moderate to low-angle faults above, below and near the detachment faults; 3) high angle reverse faults that cut the detachment fault; and 4) northwest-trending folds within the upper plate. The Lincoln Ranch fault is the major structure in the LRB. The Lincoln Ranch fault continues southeastward across the Buckskin Mountains and through the Rawhide Mountains (Spencer and Reynolds, 1989). Southeast of A-Bomb Canyon, the Lincoln Ranch fault bifurcates into two major strands that bound a block containing both lower-plate and upper-plate rocks (Spencer and Reynolds 1989).

Fault-block shapes within A-Bomb Canyon have been described and compared to physical models by Laubach et al. (1992). They found three main fault types in profile: curved faults, planar faults and faults with ramp-flat geometry. Curved faults and planar faults are approximately equally abundant, with curved faults being split almost evenly between concave-up and convex-up faults (Figure 5A). Planar faults are divided between domino (Figure (5C) and horst-and-graben patterns and are common at all scales. Faults containing ramp-flat geometry occur where bedding is cut by a fault at a low angle (less than 45°), and the faults oriented at a higher angle, within the range of 50° to 70°, traverse different rock types with little to no deflection (Laubach et al., 1992) (Figure 5B). The study indicates that ramp-flat geometry faults

tend to cut at higher angle through the sandstone layers and flatten in siltstone layers (Laubach et al., 1992).

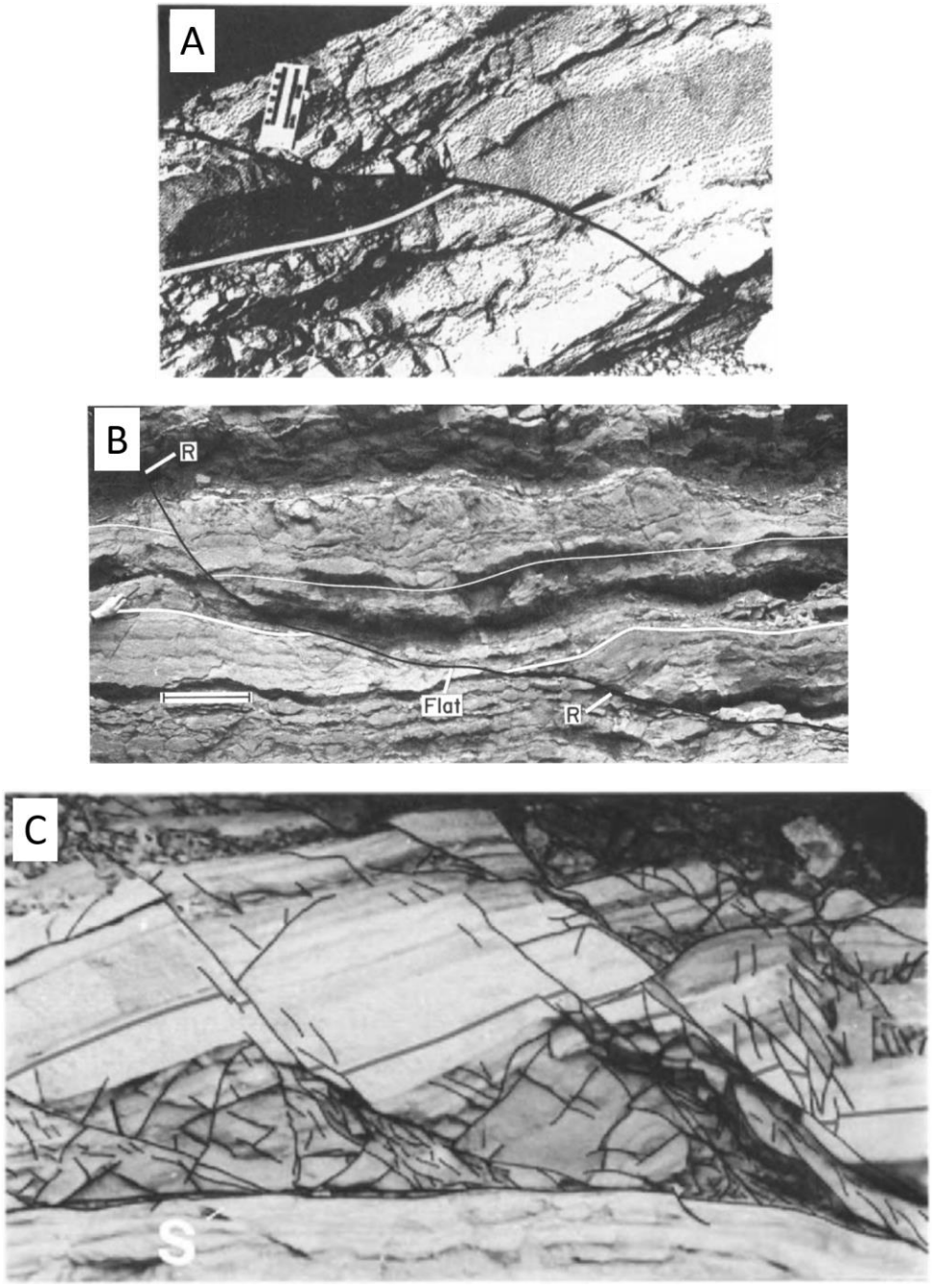

Figure 5: A) Curved fault geometry in cross-section view. Scale is in centimeters. B) Ramp-flat geometry in cross-section view. Scale is 10 centimeters. C) Planar (domino) fault geometry in cross-section view. Width of tilted fault block seen in the center of the photograph is 10 centimeters. Photographs from Laubach and others (1992).

Section 4. Methods

This thesis examines two complementary yet independent categories of quantitative fault observations: position and displacement (hereafter "size"). Size-distribution analysis of fault displacement ignores fracture position, apart from occurrence somewhere on a common scanline. In contrast, descriptive statistics of spatial arrangement (e.g., Cv, ratio of standard deviation to mean of nearest-neighbor fracture spacings) address fracture positions but not displacements, apart from a size threshold for detection on a common scanline. This thesis considers both categories of analytical metrics for a single data set. Specifically, overlapping scanlines that use four different thresholds of fault displacement quantify both position and displacement, and they meet requirements for both types of analysis.

FIELD METHODS

One-dimensional sampling of displacement discontinuities has previously been used to study joints (e.g. La Pointe and Hudson, 1985), veins (e.g. Marrett et al., 1999) and faults (e.g. Barton, 1995; Watterson et al., 1996). This study used one-dimensional scanlines along the floor and walls of A-Bomb Canyon. Scanline collections utilized four different thresholds (resolutions) for fault detection. In each case, scanline data consisted of displacement and position measurements for all faults having displacements greater than or equal to a pre-determined threshold of minimum displacement.

A nearly kilometer-length scanline assessed fault displacement and position for faults having displacements greater than or equal to one meter (Scanline A; Figure 6A). A complementary, high-resolution, scanline of ~125 m included all faults having displacement of one centimeter or more (Scanline C), which was decimated or reduced to form another dataset of faults with displacement of ≥ 10 cm (Scanline B). The fourth scanline (measuring ~12 m in length) included all faults having displacement of one millimeter or more (Scanline D, Figure 6B).

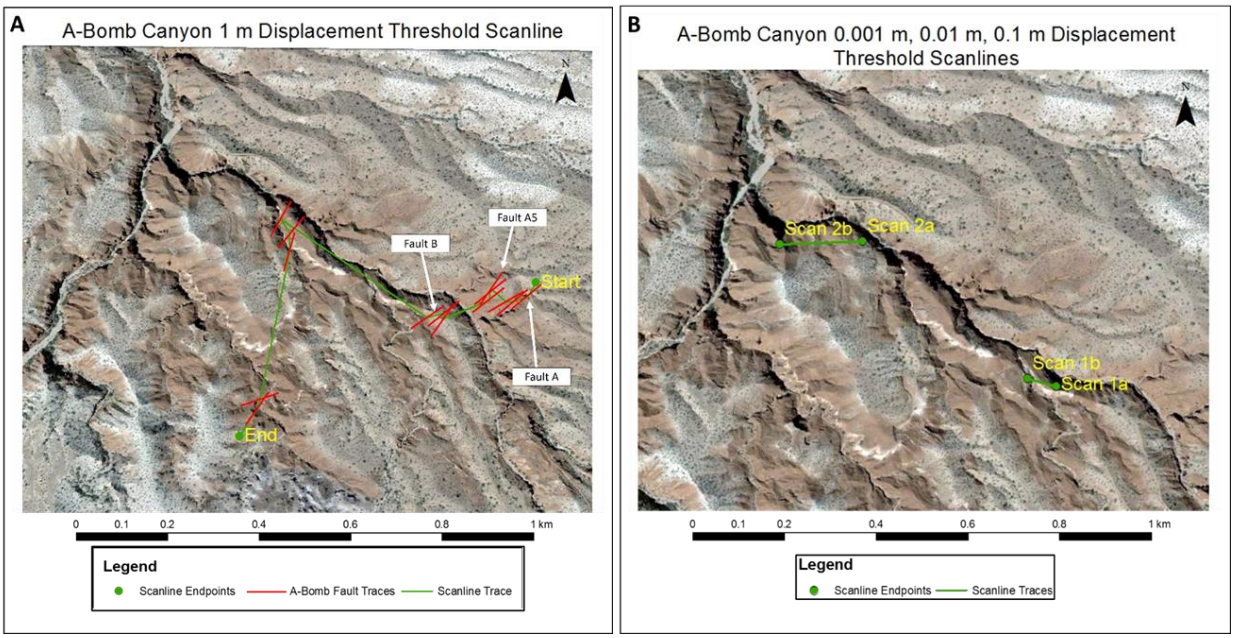

Figure 6: Two aerial images of A-Bomb Canyon. Image extents approximately correlate with extents of Figure 1B. A) Location of the > 1 meter displacement faults (red) that intersect Scanline A (green). B) Scanline pathways encompassing Scanlines B, C, and D can be seen in GREEN. These are in two sections: "Scan 1" and "Scan 2", which are clearly depicted with "a" labels denoting the start of the scanline and "b" labels denoting the end of the scanline. Scan 2 is the location of Scanlines B and C, Scan 1 is the location of Scanline D.

Scanlines with displacement thresholds of 1 millimeter, 1 centimeter, and 10 centimeters were collected within A-Bomb Canyon itself on the canyon walls, where there is excellent exposure of the Miocene aged sandstones that are clearly layered and allow for precise measurement of the fault displacements. The 1 meter displacement threshold scanline was collected on the canyon wall and across the field area, where the exposure is similar to the exposure of the other three scanlines (Figure 6).

Fracture positions on all scanlines were surveyed with a tape measure and Brunton compass. A tape measure determined the minimum layer-parallel distance between nearest-neighbor faults, in order to follow layering from one fault to the next. A Brunton compass was used to measure scanline azimuth and plunge. Compass measurements were used to make trigonometric corrections so that distance measurements corresponded to layer-parallel, cross-strike spacing between faults. Consequently, serial addition of fault spacing yields the position of each fault relative to the origin of the scanline. The tape and Brunton measurements mentioned above form the raw data (Appendix A, B, and C) for analysis of spatial arrangement.

A Brunton compass, tape measure and ruler assisted in characterizing the 571 faults that met the predetermined thresholds of displacement along the scanlines. The tape measure provided a precision of 1 centimeter for fault displacements along Scanline A (displacement threshold of 1 meter). The larger displacements (≥ 1 meter) faults were distinguished using displacements of stratigraphic layers. The distinct white tuff layers and conglomerate layer allowed for measurement of the displacement of the largest faults.

Displacements on Scanline C (displacement threshold of 1 centimeter) were determined by displacements of the intraformational beds to a precision of 1 millimeter used a tape measure and a ruler. Lastly, displacements on Scanline D, with a displacement threshold of 1 millimeter, were also determined by displacements of the intraformational beds to a precision of 1 millimeter.

Fault surface and slip lineation orientation where exposed were measured for 33 faults with a Brunton compass (Appendix D). Equal-area stereonet allows visualization of fault orientations along the scanlines (Figure 7).

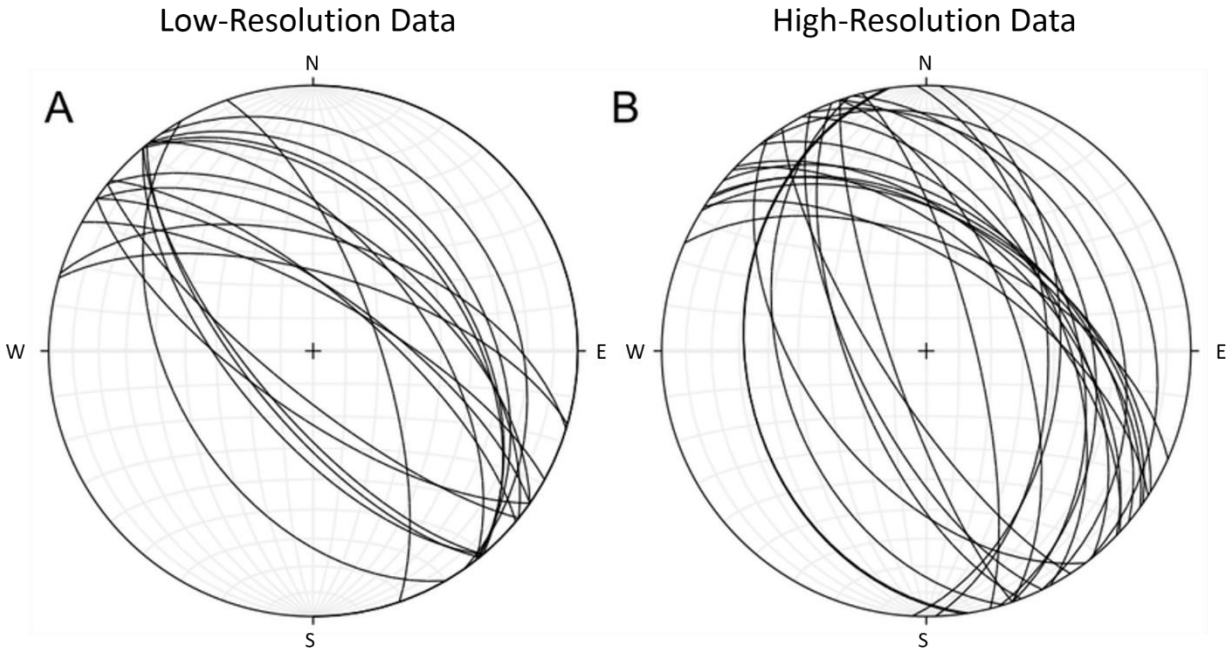

Figure 7: Stereonets showing characteristic fault orientation data collected from each scanline. A) Stereonet representation of Low-Resolution fault orientations for 19 faults. NE dipping synthetic faults are the dominant faults. B) Stereonet of representative sample (25 faults) of High-Resolution fault orientations. The dipping synthetic faults are the dominant fault orientation.

Scanline techniques of this study are equivalent to studies of spatial arrangement conducted on bedding-parallel fractures in shales (Gale et al., 2015; 2016), naturally occurring fractures in shales (Gale et al., 2014), deformation bands (Gibbons, 2006), opening mode fractures (Gomez, 2007) and other fracture types.

ANALYSIS OF FAULT DISPLACEMENT

Fault size distribution analysis of a group of related faults consists of determining the cumulative frequency for each fault displacement and comparing that to fault length or displacement. Ordering faults in a list of descending displacement from largest to smallest achieves this comparison. Once ordered, faults were assigned a number, beginning with 1 and moving down a descending list of fault sizes by increments of 1 (ex., 1, 2, 3…) until each fault size has an associated (or cumulative) number. Instances of duplicate displacement values (due to the finite scale of observations) were eliminated (leaving only the highest cumulative number) to eliminate sampling artifacts. Dividing the cumulative number assigned to each fault displacement by the total length of the scanline provided the cumulative frequency or fracture intensity. The displacement value of each fault size was then compared graphically to the associated cumulative frequency to visualize the size distribution of the fault population. Least-squares regression analysis determined the best-fit for the data.

Marrett et al. (1999) studied the power-law scaling of natural rock fractures, using datasets from the Ozona Sandstone, Marble Falls Limestone, and the Paintbrush Group tuff. They found power-laws across at least 3-5 orders of displacement magnitude. This consistency was observed independently on multiple scanlines of different resolutions and among different lithologies. Fracture type as a possible limitation to power-law scaling was examined. It was determined that fractures having opening (Ozona Sandstone and Marble Falls Limestone) and shear (Paintbrush Group) displacements are similar with respect to scaling. The simple linearity exhibited in the log-log graphs in the previous work is consistent with the idea that displacements along brittle fractures can be characterized as a single fractal across a wide range of scales.

Hooker et al. (2014) identified a narrow range of universal power-law exponents for opening-mode fracture apertures in sandstones. In a study utilizing nearly 4,000 fractures over 68 scanlines spanning eight formations on three continents, they found that lower values of the power-law scaling exponent represent a gradual increase in the frequency of fractures as fracture size decreases. Power-law exponents, measured in one-dimensional (scanline) samples, typically

exhibited values ranging from -0.8 ± 0.1. The majority of variation amongst fracture sets resulted from the power-law coefficients, a scale-invariant measure of fracture intensity (Ortega et al., 2006). The power-law exponents for the size distribution of the A-Bomb fracture datasets can be compared to this reported range of -0.8 ± 0.1. Whereas Hooker et al. (2014) focused on opening-mode fractures in distributed, parallel sets, this thesis addresses shear fractures that form conjugate pairs.

Analysis of Spatial Arrangement

The spatial arrangement of natural fractures is examined here to understand whether fractures are systematically clustered, randomly arranged, or anti-clustered (regularly spaced)—the only logical possibilities for the arrangement of discrete features along a scanline. The coefficient of variation provides a useful estimate of this characteristic and is determined by the ratio of standard deviation to mean of nearest-neighbor spacings (e.g., Gillespie et al., 1993). If the coefficient of variation is near 1, then the fractures are randomly arranged. If the coefficient of variation is greater than 1, then the fractures display a clustering effect (e.g. Hooker et al., 2014). A coefficient of variation less than 1 indicates anti-clustering (Gillespie et al., 1993). Like other traditional methods of spacing analysis, the sequence in which spacings occur along a scanline is ignored by the coefficient of variation and limits its utility (Gomez and Marrett, in review). As a consequence, the spatial arrangement of fractures at A-Bomb Canyon will be assessed using not only the coefficient of variation but also the correlation count approach, which embraces the sequence of spacings.

The correlation count technique (Marrett et al., in review) overcomes the limitations of traditional analyses by analyzing fracture positions along a scanline, rather than nearest-neighbor spacings alone. The distances between each pair of fractures in a dataset (including but not limited to nearest neighbors) are analyzed. Using all possible fracture pairs in the analysis implicitly accounts for the sequence of spacings along the scanline, because any modification of the sequence would cause a change in a significant number of distances between fracture pairs.

Following procedures in Marrett et al. (in review), the correlation count (c) quantifies the fraction of all fracture pairs that are separated by a distance between two values of length scale ($\lambda k+m$ and $\lambda k-m$):

$$c(\lambda_k) = \frac{2}{N(N-1)} \sum_{i=1}^{N} \sum_{j=i+1}^{N} H\left[\lambda_{k+m} - (x_j - y_i)\right] - H\left[\lambda_{k-m} - (x_j - y_i)\right]$$

where N is the number of fractures in the scanline, (xj – yi) is the separation between the ith and jth fractures, H is the Heaviside step function, and m is adjustable. If fracture positions are random (i.e., equally likely to be located at any position along the scanline), then the correlation count (crandom) will depend only on the length of the scanline (L) and the length scales considered.

$$c_{random}(\lambda_k) = \frac{\lambda_{k+m} - \lambda_{k-m}}{L}\left(2 - \frac{\lambda_{k+m} + \lambda_{k-m}}{L}\right)$$

Normalizing the observed correlation count with the expected correlation count for randomly positioned fractures yields a measure of spatial correlation that varies as a function of length scale. Like the coefficient of variation, the NCC exceeds 1 for fracture-to-fracture distances (length scales) that are more abundant in the observed arrangement than in a random arrangement, and NCC less than 1 indicates fracture-fracture distances that occur less frequently than random in the observed arrangement.

NCC varies according to length scale in certain distinct patterns that quantify spatial arrangement (Marrett et al., in review; Figure 8). The spatial arrangement of fractures that is indistinguishable from random has NCC near one for all length scales (Figure 8A). Approximately regularly spaced fractures, or fracture clusters with regular spacing, show peaks of NCC greater than one at a length scale corresponding to the prevailing fracture/cluster spacing and its integer multiples, and troughs of NCC less than one at intermediate length scales (Figure 8E, 8G). Fractal clusters of fractures (i.e., self-organized) show NCC > 1 that follows a power law as a function of the shortest length scales (Figure 8D). Maintaining a NCC value greater than one constantly across as wide range of length scales defines a plateau pattern due to inherited or externally imposed clusters (Figure 8B). A pattern dominated by NCC across one range of length scales and a different prevailing model of NCC over a complimentary range of length scales indicates that combinations of the patterns coexist.

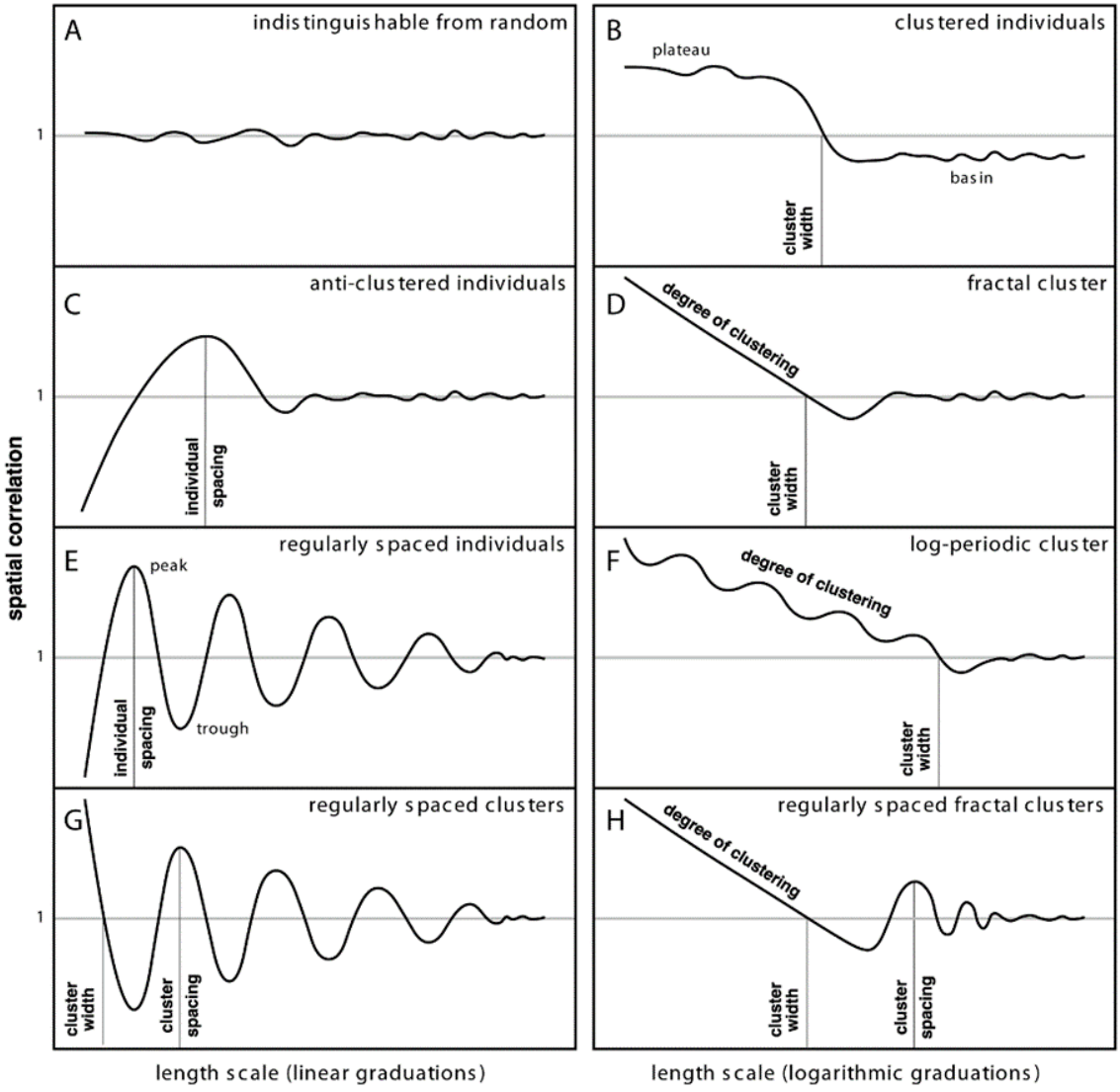

Figure 8: Variation of spatial correlation with length scale plotted linearly and logarithmically, and interpretation of some patterns (from Marrett et al., in review). A flat-line pattern of spatial correlation (slope = 0; correlation = 1, A) indicates no statistically significant organization. Power-law variation of spatial correlation with length scale (slope ≠ 0); best appreciated with logarithmic graduations of length scale, D) indicates fractal clustering, one form of self organization. A plateau-and-basin pattern (B) of spatial correlation (slope = 0; correlation ≠ 1) indicates statistically significant clustering, due to some process other than self organization such as inherited or externally imposed control. Periodic peaks and troughs (best appreciated with linear graduations of length scale, E) indicate regular spacing, another form of self organization. Combinations of any or all of these patterns can occur, with different patterns characterizing different ranges of length scale.

95% confidence intervals are presented in NCC plots. Confidence intervals are calculated within the CorrCount program (https://github.com/marrett/CorrelationCount). This is done by Monte Carlo simulation of the data, where CorrCount uses a random number generator to artificially relocate the faults. Relocation is done a specific number of times defined by the user, in order to create spatially randomized versions of the input data. The program then calculates the NCC for each set of randomized fault locations at each specific length scale, as done for observed fault locations. For analyses of randomized fault locations, the NCC's are averaged at each length scale and standard deviations are calculated, from which the 95% confidence intervals and the mean can be plotted as functions of length scale.

Section 5. Results

This section presents data collected during this study. Data include both qualitative and quantitative observations. Qualitative observations include the general characteristics of faults, and the geometry of faults in cross section and in map view. Quantitative observations include fault orientations and kinematics in the scanline datasets. Locations of scanline start and end points and the location of faults having displacement > 1 meter are shown in Figure 6.

General Characteristics of the Faults

Faults examined have displacements of millimeters to at least 32 meters. Faults have both curved and planar surfaces. Nearest-neighbor spacings between faults ranged from a couple hundred meters for the largest faults, tens of meters for faults with approximately 1-2 m displacements, and to centimeters for the smallest of faults.

Fault Orientations

The majority of the fault planes in this study have NW and SE strikes (Figure 7). Faults dip NE and SW (Figure 7). Northeast dips are considered synthetic as they follow the NE directed displacement of the underlying detachment fault (Spencer and Reynolds, 1991). Southwest dipping faults are antithetic for the purpose of this study, as their displacement direction is contrary to the detachment fault.

Scanline C contains 486 faults, of which there are 300 synthetic faults. Scanline A contains 19 faults, of which 13 are synthetic. Thus, a majority (62%) of the faults included in the high-resolution scanline and a majority (68%) of the faults included in the low-resolution scanline are synthetic.

Geometry of Faults

Past studies have stated that most of the moderate-angle normal faults were northwest trending (Spencer and Reynolds, 1989). The normal faults observed in the field were found to have a northwest strike averaging 309o (Figure 7). Faults of meter-scale displacement scale are planar (Laubach et al., 1992). Smaller displacement faults are at relatively high angles to bedding and have northwest strikes and dominantly northeast dips (Figure 7b).

Faults in Map View

Faults in map view show a variety of geometries (Figure 6). Fault traces are straight, curved or a combination of the two. Absent are faults that strike parallel to the direction of extension, so transfer faults are not important. Faults generally terminate along strike by intersecting another fault or by progressively losing slip; both types of fault terminations were observed and are visible in map view. Fault tip splays, although not observed on all faults, are developed near some fault tips.

FAULT KINEMATICS

Fault slip lineation data were organized and represented graphically using FaultKin (Allmendinger, 1992) (Figure 9). Consistent with the regional tectonic regime and earlier findings (Singleton, 2015), no evidence of reverse or strike-slip movement was found along the scanlines (Figure 9). Faultkin analysis produces values of a 54.1° trend and a 1.3° plunge for kinematic axis 1, a 324.1° trend and a 2.0° plunge for kinematic axis 2 and a 178.4° trend and a 87.6° plunge for kinematic axis 3 for the fault slip lineation recorded on faults from A-Bomb Canyon.

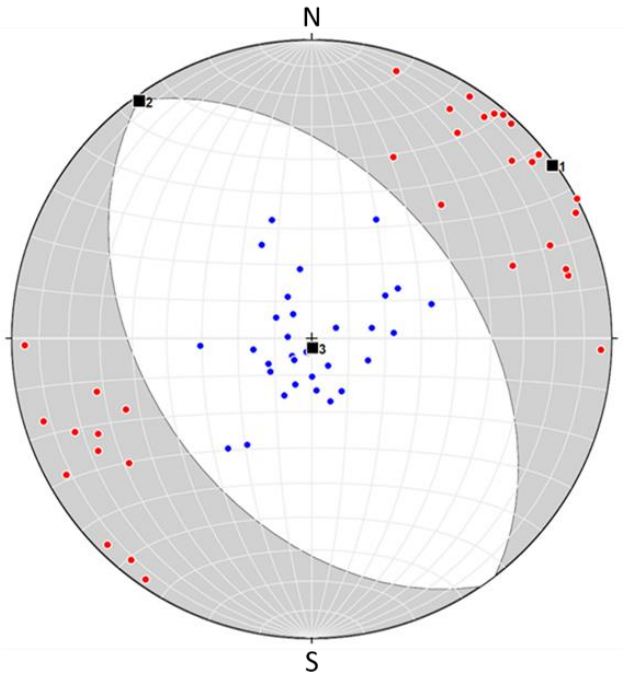

Figure 9: Stereogram (lower hemisphere, equal area net) displaying kinematic analysis of faults (N = 33) from A-Bomb Canyon. Filled dots indicate principal directions of infinitesimal strain determined for each fault, red for maximum extension and blue for maximum shortening. Linked Bingham analysis of the fault population estimates a (spatially) averaged tensor for infinitesimal strain, illustrated by black squares (1 is maximum principal extension; 2 is intermediate principal extension; 3 is minimum principal extension), and great circles (planes of zero longitudinal strain). Shading marks dihedra having positive extension, making the diagram resemble a focal mechanism for an earthquake. Kinematic axis 1 has a trend of 54.1° and a plunge of 1.3°. Kinematic axis 2 has a trend of 324.1° and a plunge of 2.0°. Kinematic axis 3 has a trend of 178.4° and a plung of 87.6°.

Section 6. Analysis

Scanlines B and C have the same length but different numbers of faults (Table 1). The difference in fault abundance is because the same scanline tract was used initially for all faults with a displacement greater than 0.01 meters, which constituted the data for scanline C. Scanline C's data were then decimated (subsampled) to only include faults with a displacements greater than 0.1 meter to create the dataset for scanline B. Scanline D was collected over the first 12.1 meters of the scanline tract ("Scan 1" in Figure 6) that defines scanlines B and C and focused on faults with displacements greater than 0.001 meters. These datasets were then analyzed for their displacement distributions and spatial arrangement.

Scanline	Displacement Threshold (m)	Number of Faults	Scanline Length (m)
A	1	19	751
B	0.1	60	125
C	0.01	431	125
D	0.001	121	12.1

Table 1: Scanlines and the associated displacement thresholds.

DISTRIBUTION OF FAULT DISPLACEMENTS

The displacement distribution of the faults in the four datasets were examined separately and then compared graphically. In order to graphically display the displacement distribution of the faults, the cumulative frequency, which is synonymous with fracture abundance and defined as intensity, was compared against the displacement values of the faults.

1 Millimeter (0.001 Meter) Displacement Threshold

Scanline D has 121 faults of less than 10 mm and greater than or equal to 1 mm displacement along a total scanline length of 12.1 meters. The size distribution exhibits a strong log-log linear trend, described by a negative power-law (Figure 10) function with a coefficient of determination (R2) of 0.941. This evidence of a strong linear trend following a power-law distribution supports previous work (Marrett et al., 1999) that brittle fracture displacements, in this case normal faults, can be characterized as a single fractal across a wide range of scales including at this smallest of scales. The power-law exponent of the highest-resolution dataset is -0.618, which falls outside the range of -0.8±0.1 that Hooker et al. (2014) found for opening-mode fractures in sandstones.

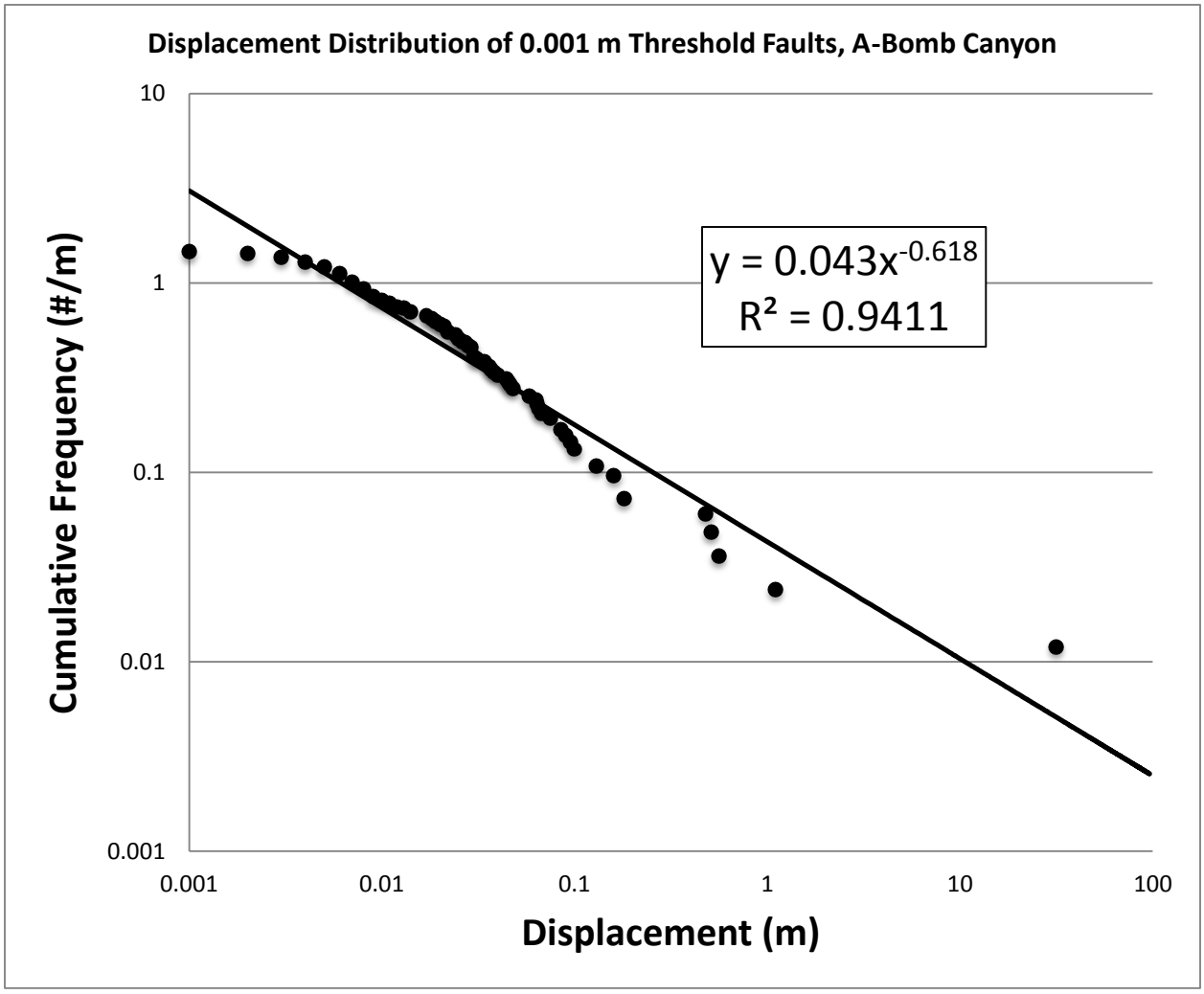

Figure 10: Log-log plot of Scanline D (0.001 m threshold) size distribution. Graph points show displacement values (X-Axis) and their associated cumulative frequencies (Y-Axis) for each fault included on the scanline. Data fit a power-law distribution (R2 = 0.9411) with an exponent of -0.618.

1 Centimeter (0.01 Meter) Displacement Threshold

Scanline C has 431 faults of less than 10 mm and greater than or equal to 1 mm displacement along the length of 125 meters. The size distribution again exhibits a strong log-log linear trend, described by a power-law, (Figure 11) with a high coefficient of determination (R2) of 0.984. The power-law exponent of the second highest-resolution dataset is -0.866, which falls within the range of -0.8±0.1 that Hooker et al. (2014) found for opening-mode fractures in sandstones.

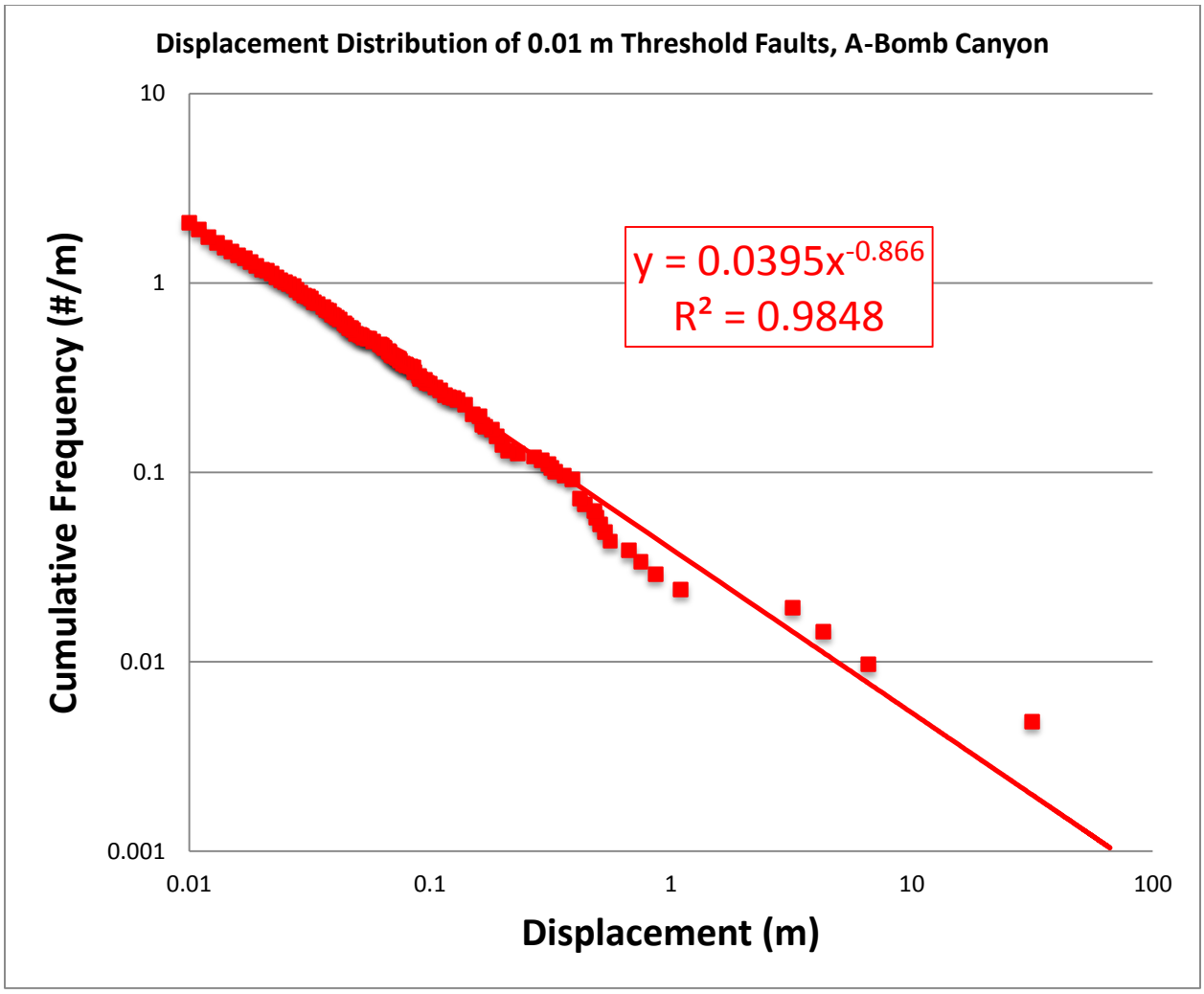

Figure 11: Log-log plot of Scanline C (0.01 m threshold) size distribution. Graph points show displacement values (X-Axis) and their associated cumulative frequencies (Y-Axis) for each fault included on the scanline. Data fit a power-law distribution (R2 = 0.9848) with an exponent of -0.866.

10 Centimeter (0.1 Meter) Displacement Threshold

Scanline B crosses 60 faults along a total length of 125 meters. This dataset was created as a subset of the second highest resolution dataset (0.01 m threshold), including only those faults with displacements less than 10 mm and greater than or equal to 1 mm. The size distribution of the 0.1 m threshold scanline exhibits a strong linear trend, described by a power-law, when plotted on a log-log plot comparing fracture abundance and fault displacement (Figure 12). The data are best fit with a negative power-law function with a high coefficient of determination (R2) of 0.953. The power-law exponent of the third highest-resolution dataset is -

0.793, which falls within the range of -0.8±0.1 that Hooker et al. (2014) found for opening-mode fractures in sandstones.

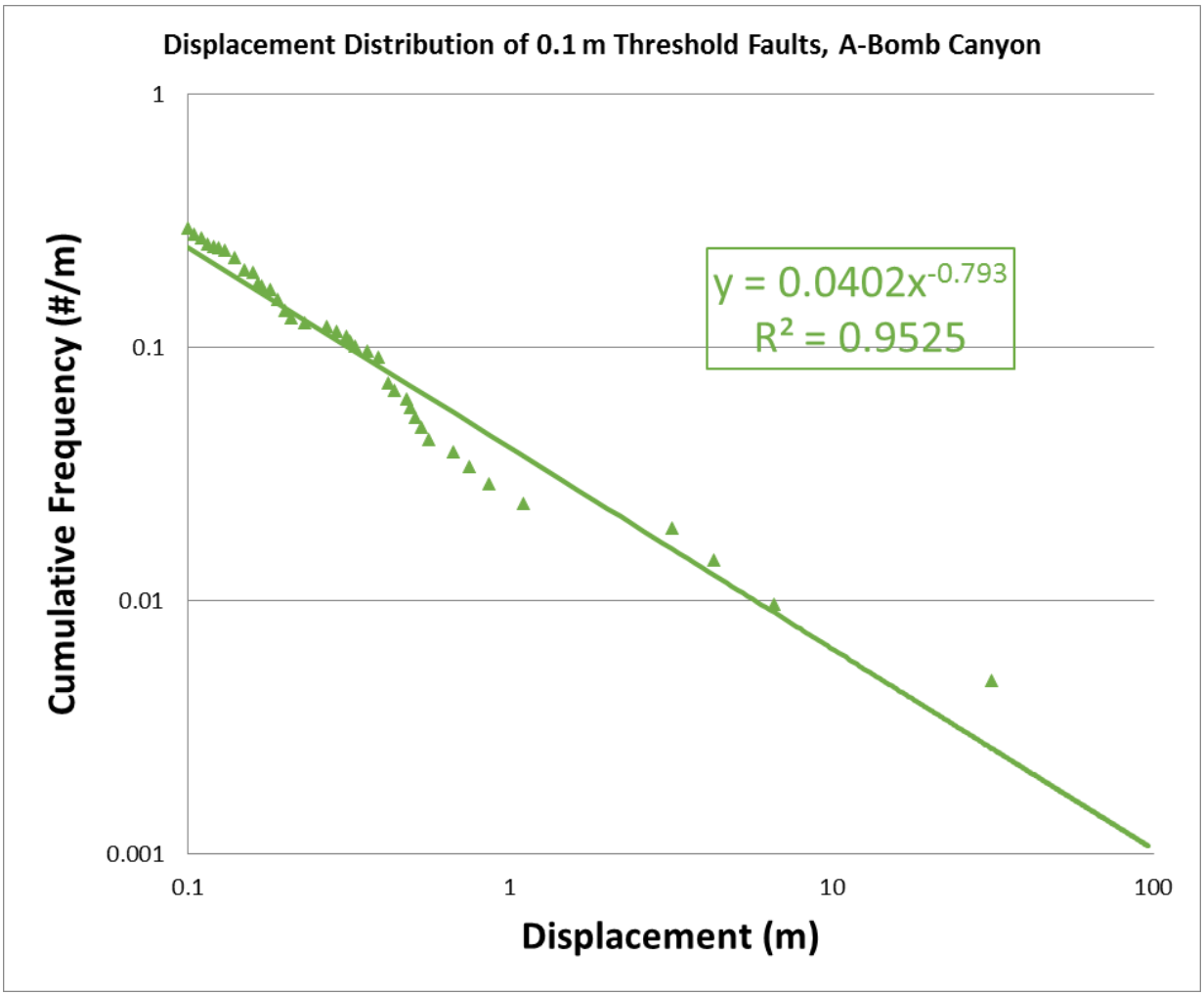

Figure 12: Log-log plot of Scanline B (0.1 m threshold) size distribution. Graph points show displacement values (X-Axis) and their associated cumulative frequencies (Y-Axis) for each fault included on the scanline. Data fit a power-law distribution (R2 = 0.9525) with an exponent of -0.793.

1 Meter Displacement Threshold

Scanline A, with a total length of 751 m, crosses 19 faults. In order to be included on this scanline, faults were required to have a displacement of ≥ 1 m. The size distribution of the 1 m threshold scanline exhibits a strong linear trend, described by a power-law, when plotted on a log-log plot comparing fracture intensity and fault displacement for each fault (Figure 13). The data are best fit with a negative power-law function with a high coefficient of determination (R2)

of 0.987. The power-law exponent of the lowest resolution dataset is 0.614, which falls outside the range of -0.8±0.1 that Hooker et al. (2014) found for opening-mode fractures in sandstones.

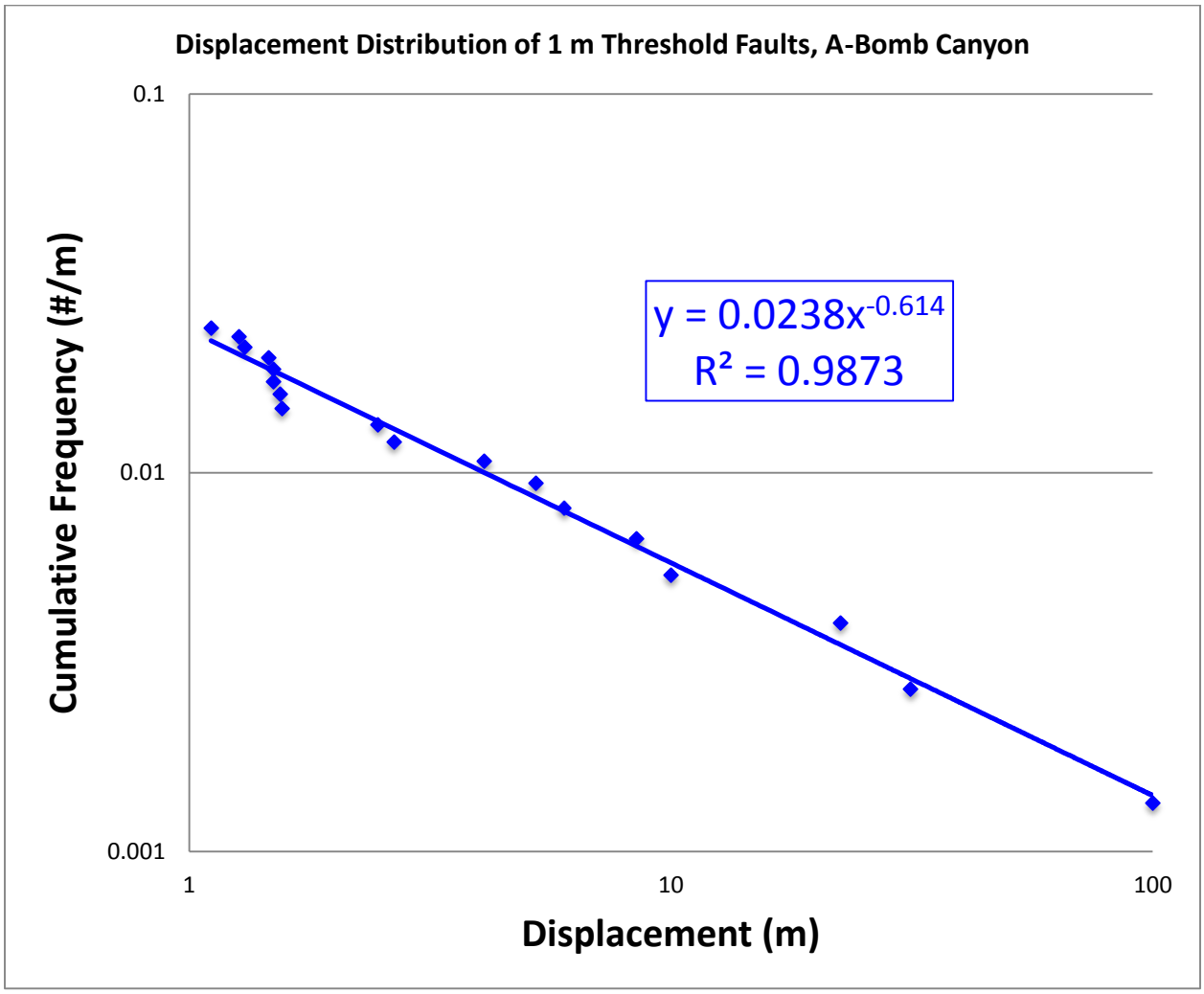

Figure 13: Log-log plot of the Scanline A (1 m threshold) size distribution. Graph points show displacement values (X-Axis) and their associated cumulative frequencies (Y-Axis) for each fault included on the scanline. Data fit a power-law distribution (R2 = 0.9873) with an exponent of -0.614.

Fault A and Fault A5 (Scanline A; Figure 6) have unknown displacements (Appendix A) because their displacements exceed the topographic relief of outcrop. Therefore, no common strata can be correlated from hanging wall to footwall. Both faults must have displacement greater than 5 m, which is the local relief of outcrop. In the case of Fault A5, displacement might minimally exceed 5 m, because sedimentary facies in adjacent hanging wall and footwall outcrops are similar. In contrast, Fault A places hanging wall Sandtrap Conglomerate against footwall Chapin Wash Formation. The depositional contact between the two map units is

everywhere eroded away from the footwall and everywhere concealed at depth in the hanging wall. As a consequence, displacement on Fault A probably is significantly more than local topography. Fault A probably has displacement that exceeds Fault B (31.5 m), ranking it as the largest-displacement fault on any scanline.

In order to best understand the size scaling of lowest resolution scanline, order-of-magnitude displacement values for these unknown values were estimated. In Figure 13, the displacement for Fault A was considered to be 100 meters, giving it the largest displacement in the low-resolution dataset, and the displacement for Fault A5 was considered to be 10 meters causing it to be the fourth largest displacement in the low-resolution dataset.

Field observations suggest that Fault A is the largest fault in the area, because it juxtaposes the Chapin Wash Formation in the footwall with the Sandtrap Conglomerate in the hanging wall. The stratigraphic contact between the two map units is exposed in neither the hanging nor footwall of Fault A. As a consequence, I consider 100 m to be a minimum estimate of displacement on Fault A. Fault A5 also yielded an "unknown" displacement that was more challenging to quantify. Fault A5 cuts only the Chapin Wash Formation in the hanging wall and footwall, so it is unlikely to have a displacement greater than Fault A, but no marker beds can be correlated unambiguously across the fault. Local exposure of the lowermost stratigraphic units along Fault A5 approximates 10 m of stratigraphic relief, so this value was taken as a minimum estimate of displacement on Fault A5.

Comparison of Scanline Displacement Distributions

Comparison of the four scanlines and their displacement distributions (Figure 14) shows a striking similarity among the datasets. The most conspicuous outliers are Fault B (displacement = 31.5 m) and faults having displacement < 5 mm. Fault B is crossed by all four scanlines, although the low-resolution dataset probably quantifies the most representative estimate of cumulative frequency. Faults having displacement < 5 mm are otherwise concordant with independent estimates of cumulative frequency for displacements ≥ 5 mm (c.f. Marrett et al., 1992). All four of the scanline datasets of varying displacement thresholds exhibit a strong power-law scaling, characterized by negative sloping power-laws (Figure 14). This similarity amongst the datasets is consistent with other similarities previously noted, such as fault orientations and fault kinematics.

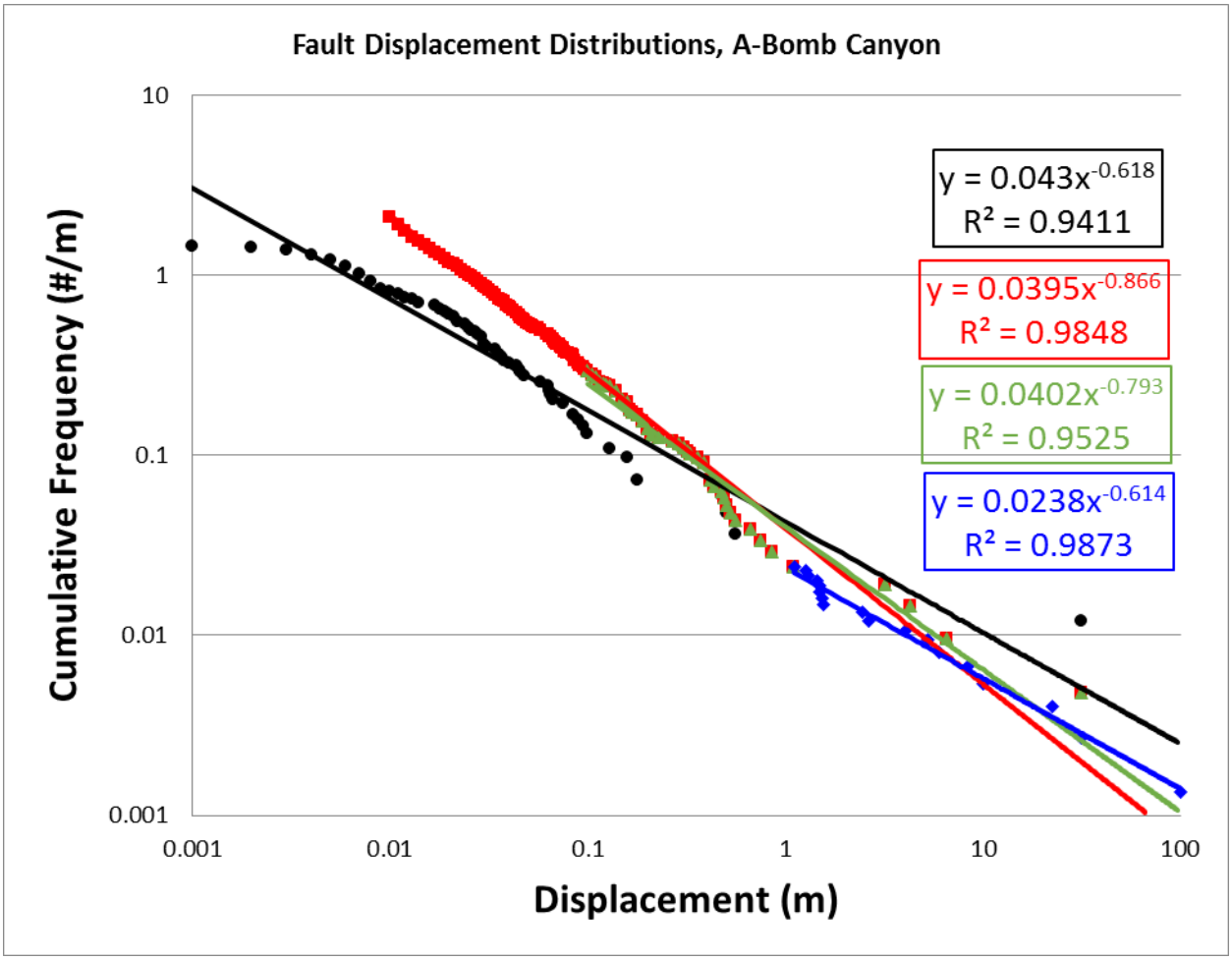

Figure 14: Log-log plot of all four fault size distributions. Graph points show displacement values (X-Axis) and their associated cumulative frequencies (Y-Axis) for each fault included on the scanlines. Data in black corresponds to the 0.001 m displacement threshold, data in red corresponds to the 0.01 m displacement threshold, data in green corresponds to the 0.1 m displacement threshold and data in blue corresponds to the 1 m displacement threshold.

Spatial Arrangement Analysis

Spatial arrangement was analyzed using the NCC method (Marrett et al., in review). Spatial arrangement analysis examines the positions of features along a scanline in order to understand whether features, in this case normal faults, are arranged randomly along the scanline or whether they display a form of clustering or anti-clustering. An indication of clustering is large Cv values (Table 2). There are several distinct patterns of NCC indicative of spatial patterns (Figure 8). Spatial arrangements were analyzed using linear-linear and log-log plots, with the former being diagnostic of characteristic periodicity and the latter characteristic of

clustering (fractal or inherited/imposed). The specific CorrCount settings used to generate each plot are listed in Table 3.

Scanline	Displacement Threshold (m)	Number of Faults (-)	Scanline Length (m)	Fracture Intensity (m-1)	Fracture Intensity (mm-1)	Cv of Spacings (-)	Mean Spacing (m)
A	1	19	751	0.025	2.5E-05	1.34	40
B	0.1	60	125	0.48	4.8E-04	1.38	2.08
C	0.01	431	125	3.45	3.45E-03	2.37	0.290
D	0.001	121	12.1	9.97	9.97E-03	1.60	0.100

Table 2: Descriptive statistics for the four scanlines.

Scanline	Displacement Threshold	NCC Log-Log Windowing	NCC Log-Log Graduation Number	NCC Linear-Linear Windowing	NCC Linear-Linear Graduation Number
A	1	2	100	1	100
B	0.1	2	100	1	300
C	0.01	1	100	1	100
D	0.001	1	100	1	100

Table 3: Windowing and length graduation settings for both the Log-Log and the Linear-Linear CorrCount analyses.

1 Millimeter (0.001 Meter) Displacement Threshold

The highest resolution data were collected along Scanline D, which crosses Fault B (estimated displacement of ~31.5 m, Appendix A), but no other mappable fault. Over a distance of 12.1 m, 121 faults have displacements of 1 mm or greater, yielding an average fracture intensity of 10 m-1 (Table 2). Only two intervals of the highest resolution scanline show statistically significant anomalies of fracture intensity. Within 7.8-9.2 m and 10.6-12.1 m (Figure 15), fracture intensity exceeds 2□ confidence limits (i.e. 20/m) and demarcates two clusters located ~3 m apart. Non-random clustering is supported by Cv of nearest-neighbor spacings, which equals 1.60 (Table 2). Note, however, that 2σ confidence limits are greater than average fracture intensity, so negative anomalies are impossible by the metric applied. As a consequence, the statistical significance of troughs in fracture abundance (e.g., within 2-7 m) cannot be measured fairly, in spite of significance at 1σ confidence.

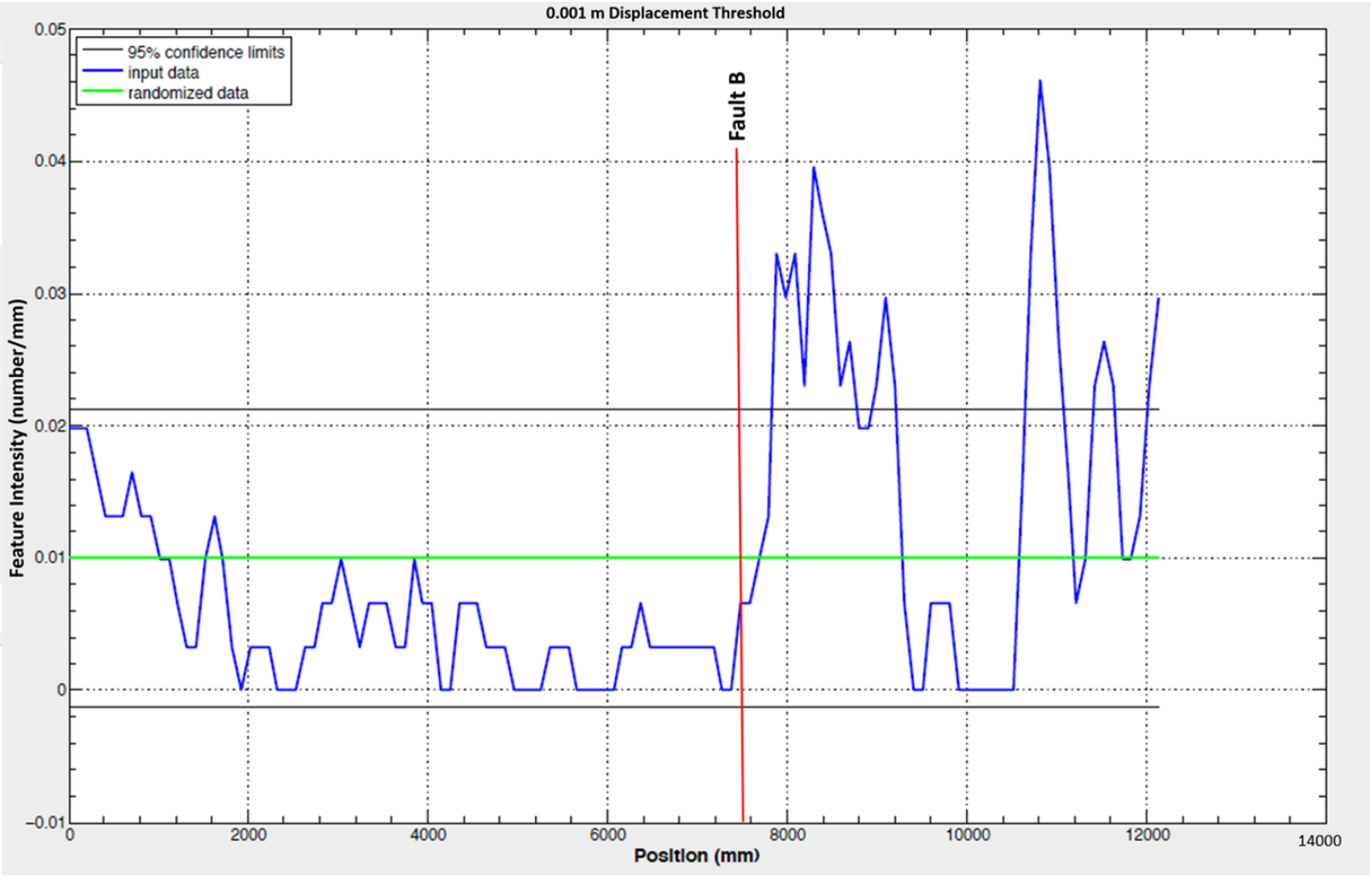

Figure 15: Intensity plot of the 1 millimeter (0.001 m) threshold dataset comparing scanline position in millimeters (X-Axis) to the fracture intensity (Y-Axis). CorrCount controls: Minimum value for length/time graduations of the intensity plot is 0 and the maximum value is 12,136 with a length/time graduation number of 121. The plot also contains a windowing value of 1. The only mappable (≥ 1 m displacement) fault included on Scanline D is Fault B, which is labeled with a red line.

The NCC of 1 mm threshold displacement data shows consistently positive anomalies for length scales below 0.8 m, regardless of whether analysis uses linear or logarithmic graduations of length scale (Figure 16 A, B). This result not only supports an interpretation of non-random clustering, it estimates cluster width to be ~0.9 m, where the NCC of the data crosses a value of 1. Analyses of NCC with both linear and logarithmic graduations of length scale show troughs between 1.3-2.2 m and a peak near ~2.8 m, a robust estimate of center-to-center distance between statistically significant clusters. Internal structure of ~0.9 m-wide clusters is described by NCC at smaller (< 0.9 m) length scales. From 0.02-0.60 m in length scale, NCC gradually decreases from 1.9 to 1.3 and approximately defines a plateau having NCC = 1.5 or follows a subtle power law having exponent – log (7/4)/log (60/2) = –1/6. These characteristics define a plateau-and-trough pattern for the 1 millimeter displacement threshold scanline.

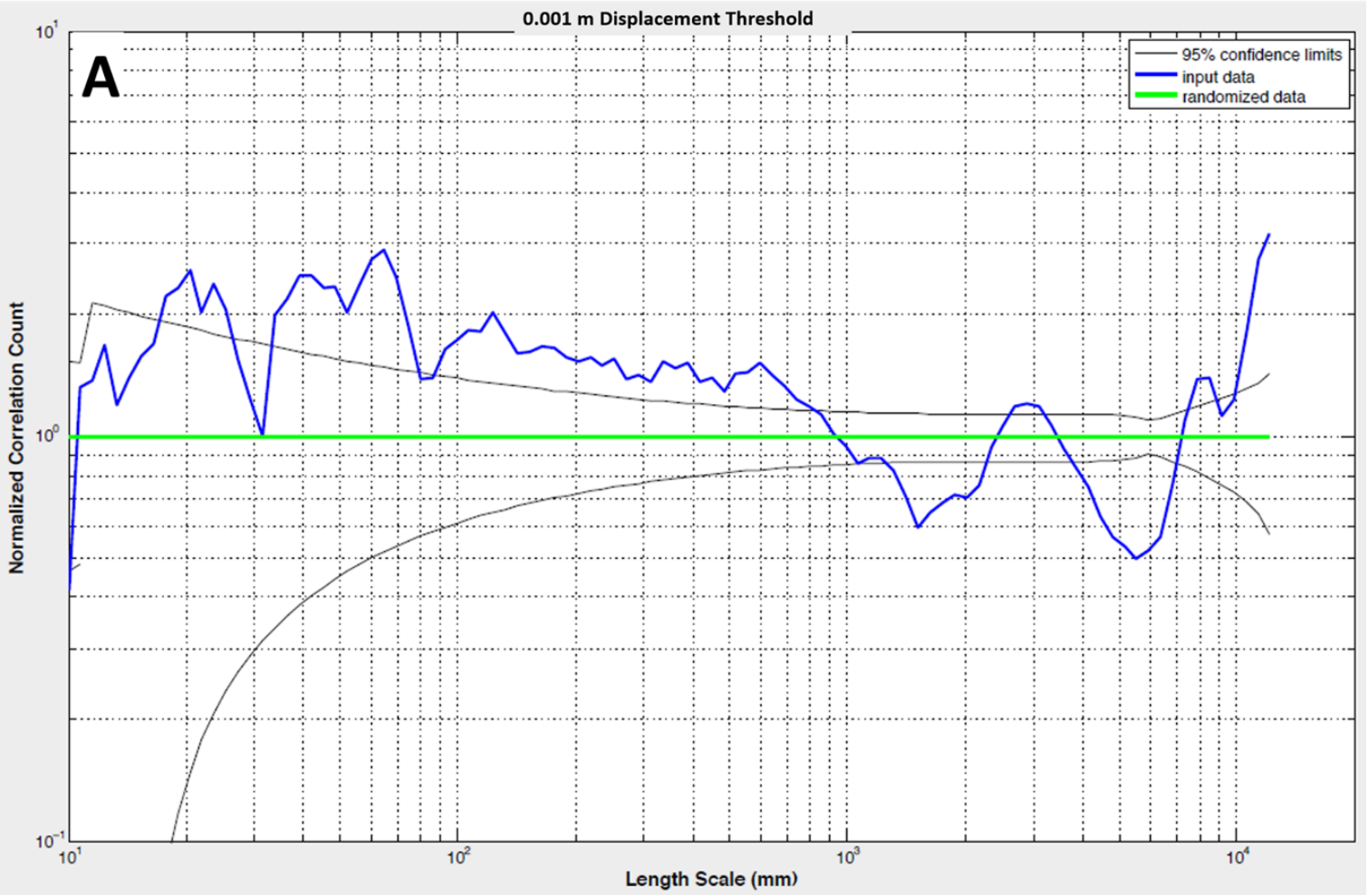

Figure 16A: NCC log-log plot of the 1 millimeter (0.001 m) threshold dataset comparing length scales in millimeters (X-Axis) to the normalized correlation count (Y-Axis).

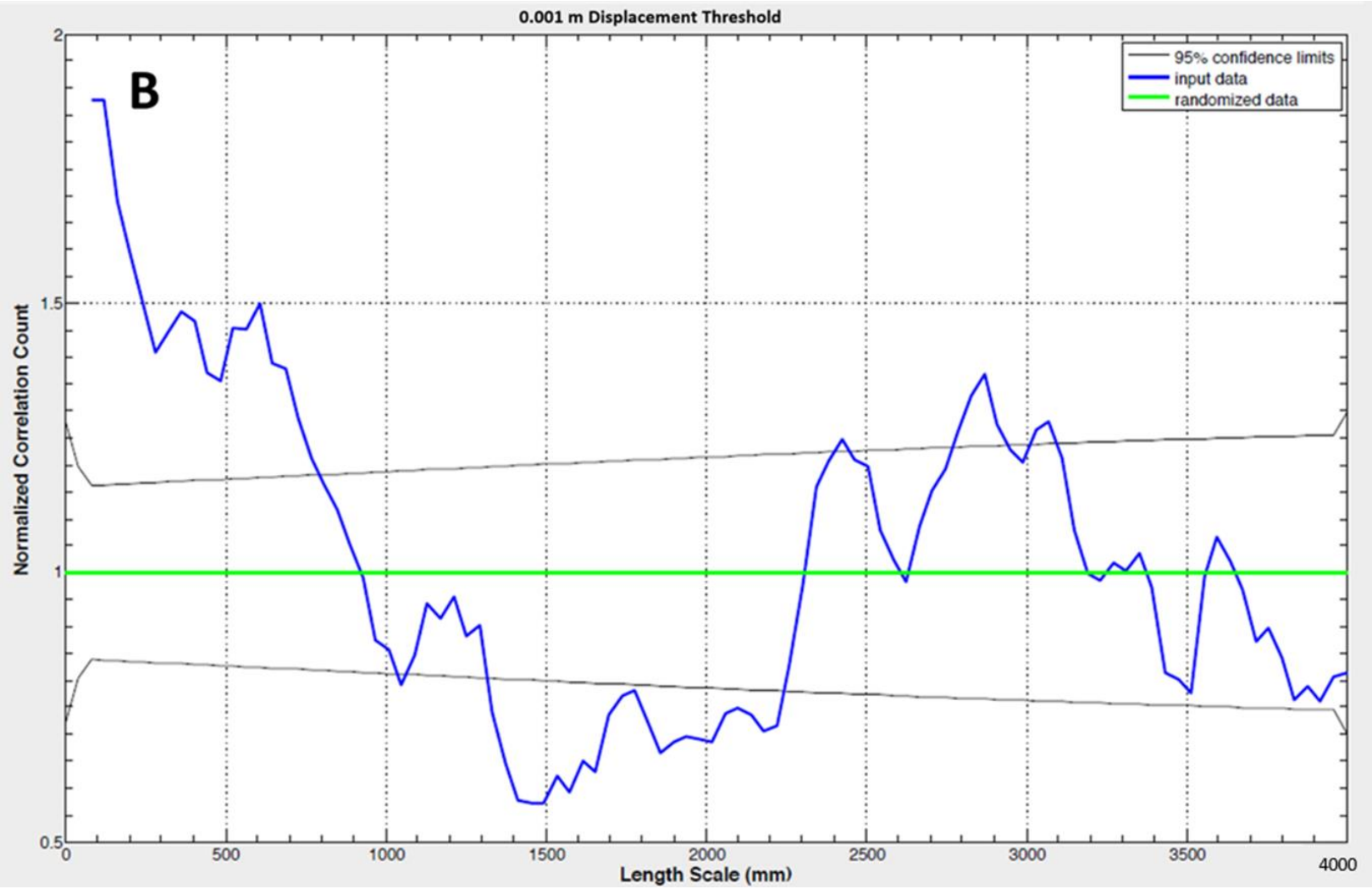

Figure 16B: NCC linear-linear plot of the 1 millimeter (0.001 m) threshold dataset comparing length scales in millimeters (X-Axis) to the normalized correlation count (Y-Axis).

1 Centimeter (0.01 Meter) Displacement Threshold

The second highest resolution data were collected along the second longest scanline segment, crossing Faults B, C, D and E. Over a distance of 125 m, 431 faults have displacements of 1 cm or greater, yielding an average fracture intensity of 3.45 m-1 (Table 2). Four intervals of scanline C show statistically significant positive anomalies in terms of fracture intensity. Within approximately 0-2 m, 6-28 m, 76-80 m, and 113-115 m (Figure 17), fracture intensity exceeds 2σ confidence limits and demarcates four spatial clusters, with nearest-neighbor spacings between the indicated clusters of 4 m, 48 m and 33 m, respectively. Non-random clustering is supported by Cv of nearest-neighbor spacings, which equals 2.37 (Table 2). There are areas along this scanline that represent statistically significant troughs, which indicates that fracture intensity is not only lower than average but lower than random. The 0.01 m scanline is the only one that exhibits these statistically significant troughs along a scanline.

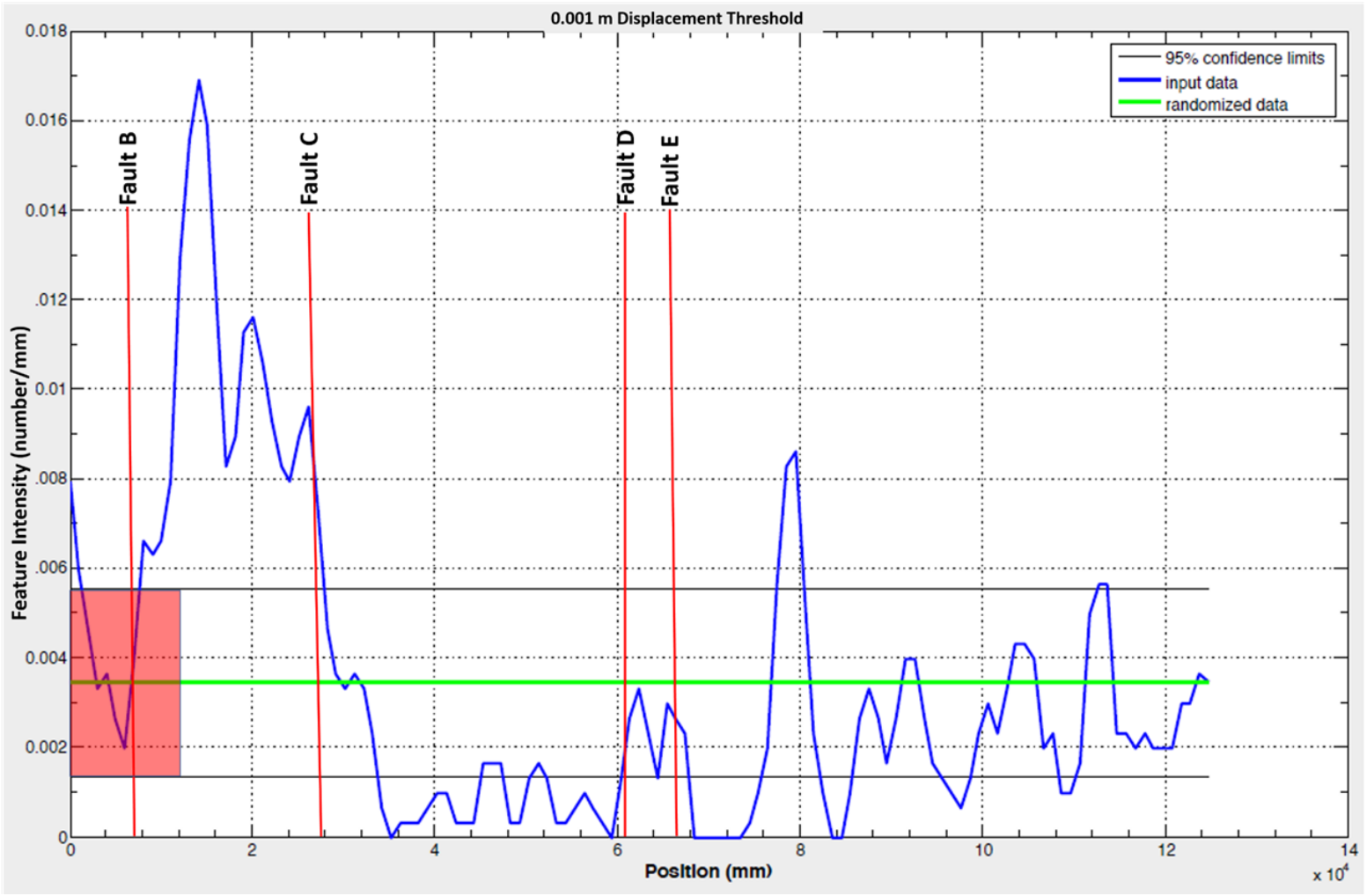

Figure 17: Intensity plot of the 1 centimeter (0.01 m) threshold dataset comparing scanline position in millimeters (X-Axis) to the fracture intensity (Y-Axis). The plot contains a windowing value of 1. Mappable (≥ 1 m displacement) faults from Scanline A are indicated and labeled by red lines. Extent of Scanline D along Scanline C is indicated by the red box extending approximately the initial 12.14 meters of the scanline length.

NCC of the 1 cm displacement data shows consistently positive anomalies for length scales below 14 m (Figure 18 A, B). This result not only supports interpretation of clustering, it estimates cluster width to be approximately 14 meters, where the NCC of the data crosses a value of 1. Analyses of NCC with logarithmic graduations of length scale shows a trough between approximately 14 m and 70 m, with a peak at approximately 100 m, a robust estimate of center-to-center distance between statistically significant clusters. These characteristics define a plateau-and-trough pattern for the 1 centimeter displacement threshold scanline.

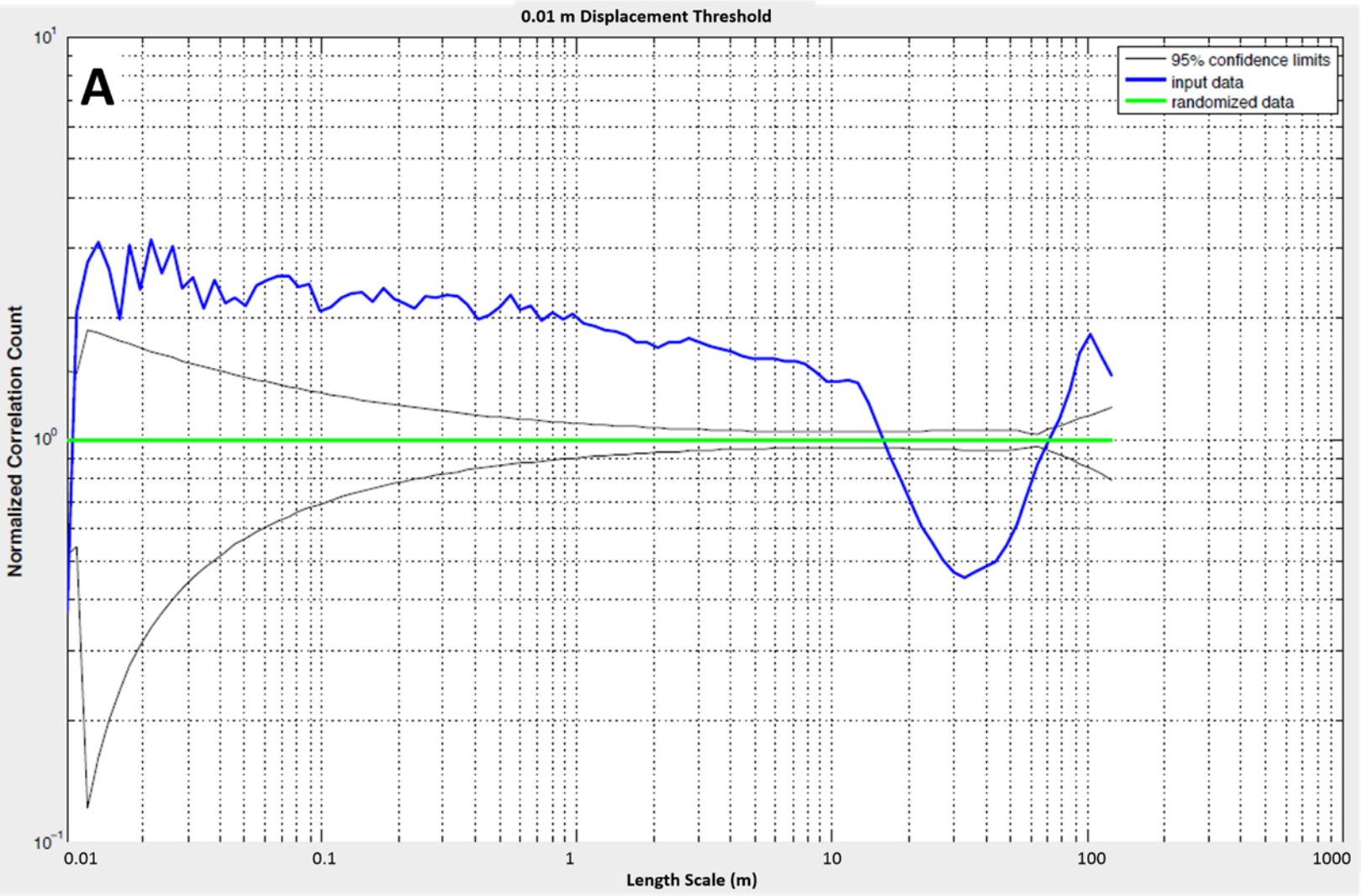

Figure 18A: NCC log-log plot of the 1 centimeter (0.01 m) threshold dataset comparing length scales in millimeters (X-Axis) to the normalized correlation count (Y-Axis).

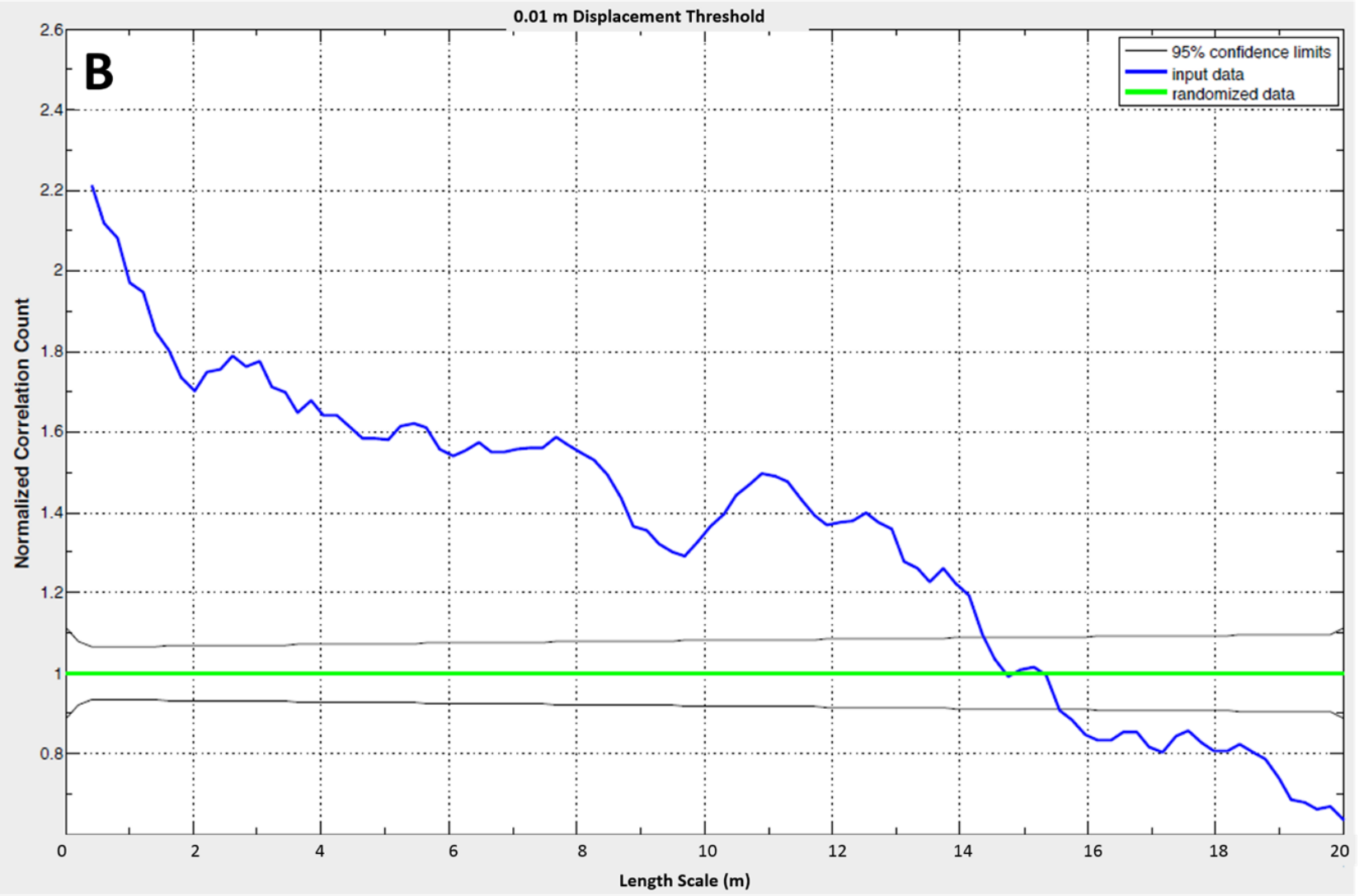

Figure 18B: NCC linear-linear plot of the 1 centimeter (0.01 m) threshold dataset comparing length scales in millimeters (X-Axis) to the normalized correlation count (Y-Axis).

10 Centimeter (0.1 Meter) Displacement Threshold

At lower resolution, the 10 cm threshold data are a subset of the cm-resolution data collected along the second longest scanline segment, which crosses Faults B, C, D and E. Over a distance of 125 m, 60 faults have displacements of between 10 and 100 cm or greater, yielding an average fracture abundance of 0.48 m-1 (Table 2). There are five interval spacings of scanline B that are statistically significant. Within approximately 2-3 m, 6-7 m, 14-18 m, 19-19.5 m and 25-30 m (Figure 19), fracture abundance exceeds 2σ confidence limits with nearest-neighbor spacings between the clusters of 3, 7, 1 and 5 m, respectively. Clustering is supported by Cv of nearest-neighbor spacings, which equals 1.38 (Table 2). Note, however, that 2σ confidence limits are greater than average fracture intensity, so negative anomalies are impossible by the metric applied. As a consequence, the statistical significance of troughs in the fracture intensity (e.g. within 32-78 m) cannot be measured fairly, in spite of significance at 1σ confidence.

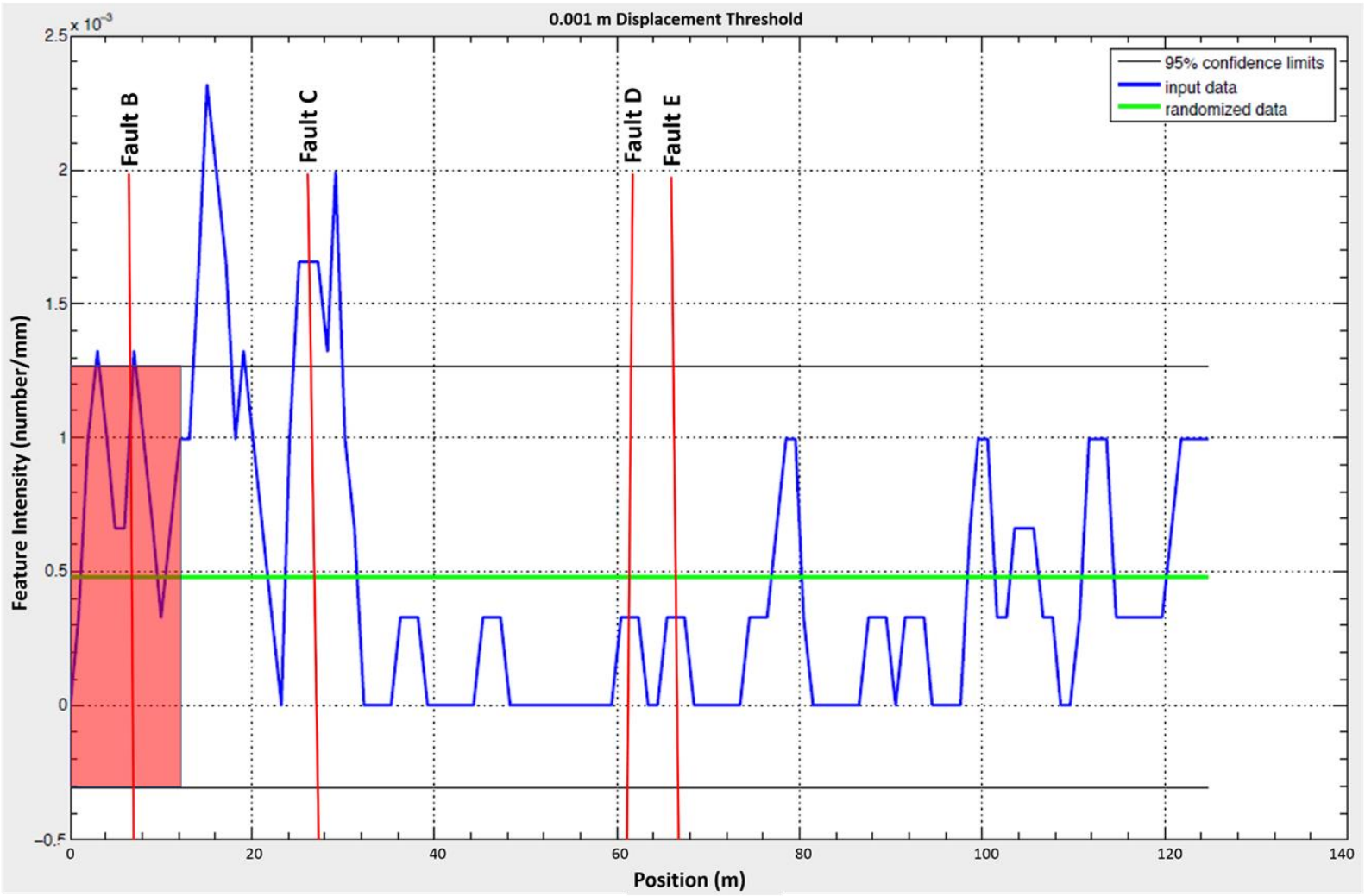

Figure 19: Intensity plot of the 10 centimeter (0.1 m) threshold dataset comparing scanline position in millimeters (X-Axis) to the fracture intensity (Y-Axis). The plot contains a windowing value of 1. Mappable (≥ 1 m displacement) faults from Scanline A are indicated and labeled by red lines. Extent of Scanline D along Scanline C is indicated by the red box extending approximately the initial 12.14 meters of the scanline length.

NCC of the 10 cm displacement data shows consistently positive anomalies for length scales below 15 m (Figure 20 A, B). This result not only supports Cv, it estimates cluster width to be approximately 15 m, where the NCC of the data crosses a value of 1. Where the data crosses at approximately 15 meters, the spatial correlation goes from above the upper 95% confidence limit to below the lower 95% confidence limit, indicating that this value of 15 meters is in fact a significant measure of cluster width. Spatial correlation crosses a value of 1 at approximately 5 meters as well but stays within the 95% confidence limits. Therefore, it is not a significant measure of cluster width. Analyses of NCC with logarithmic graduations of length scale shows a trough between approximately 15 m and 75 m and a peak at approximately 120 m, a robust estimate of center-to-center distance between statistically significant clusters. These characteristics define a plateau-and-trough pattern for the 10-centimeter displacement threshold scanline.

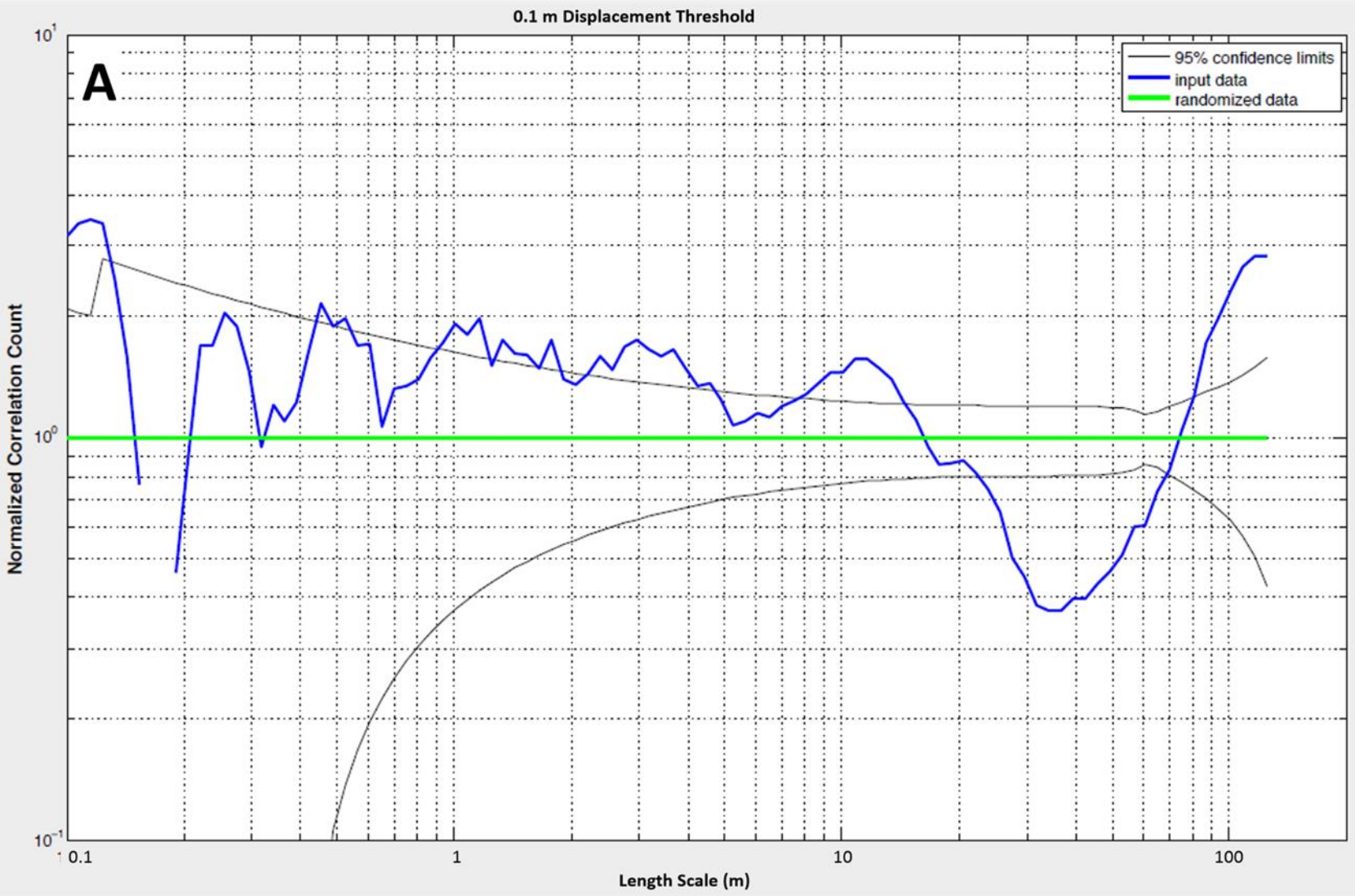

Figure 20A: NCC log-log plot of the 10 centimeter (0.1 m) threshold dataset comparing length scales in millimeters (X-Axis) to the normalized correlation count (Y-Axis).

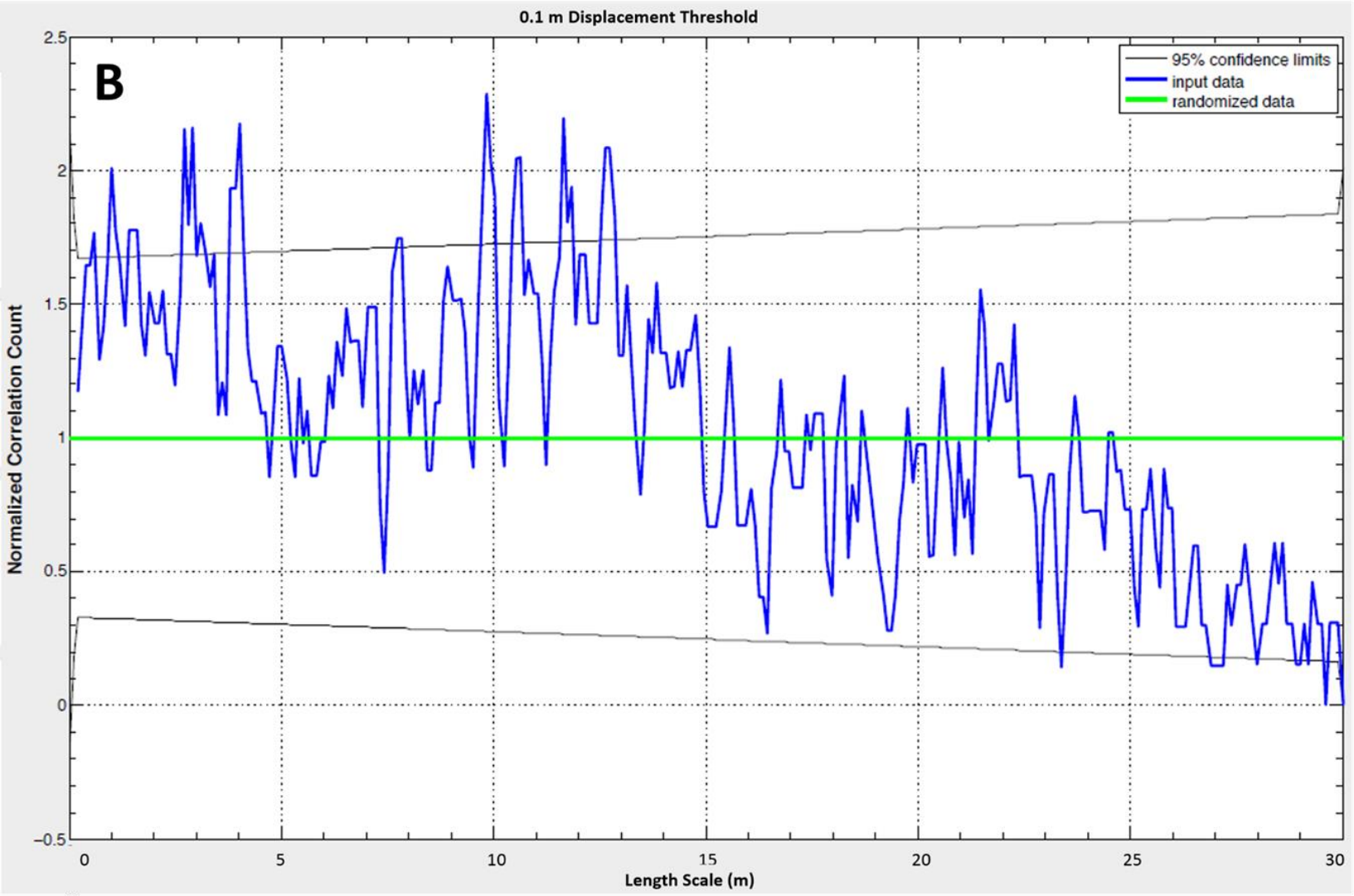

Figure 20B: NCC linear-linear plot of the 10 centimeter (0.1 m) threshold dataset comparing length scales in millimeters (X-Axis) to the normalized correlation count (Y-Axis).

1 Meter Displacement Threshold

The lowest resolution data were collected along the longest scanline, which contains all of the mappable faults. Over a distance of 751 m, 19 faults have displacements of 1 m or greater, yielding an averaged fracture abundance of 0.025 m-1 (Table 2). There are four intervals of scanline A showing statistically significant clustering. Within approximately 50-60 m, 80-90 m, 95-110 m and 200-210 m (Figure 21), fracture abundance exceeds 2σ confidence limits and defines 4 clusters with nearest-neighbor spacings between the peaks of 20 m, 5 m and 90 m, respectively. Clustering or regular spacing is supported by Cv of nearest-neighbor spacings, which equals 1.34 (Table 2). Note, however, that 2σ confidence limits are greater than average fracture intensity, so negative anomalies are impossible by the metric applied.

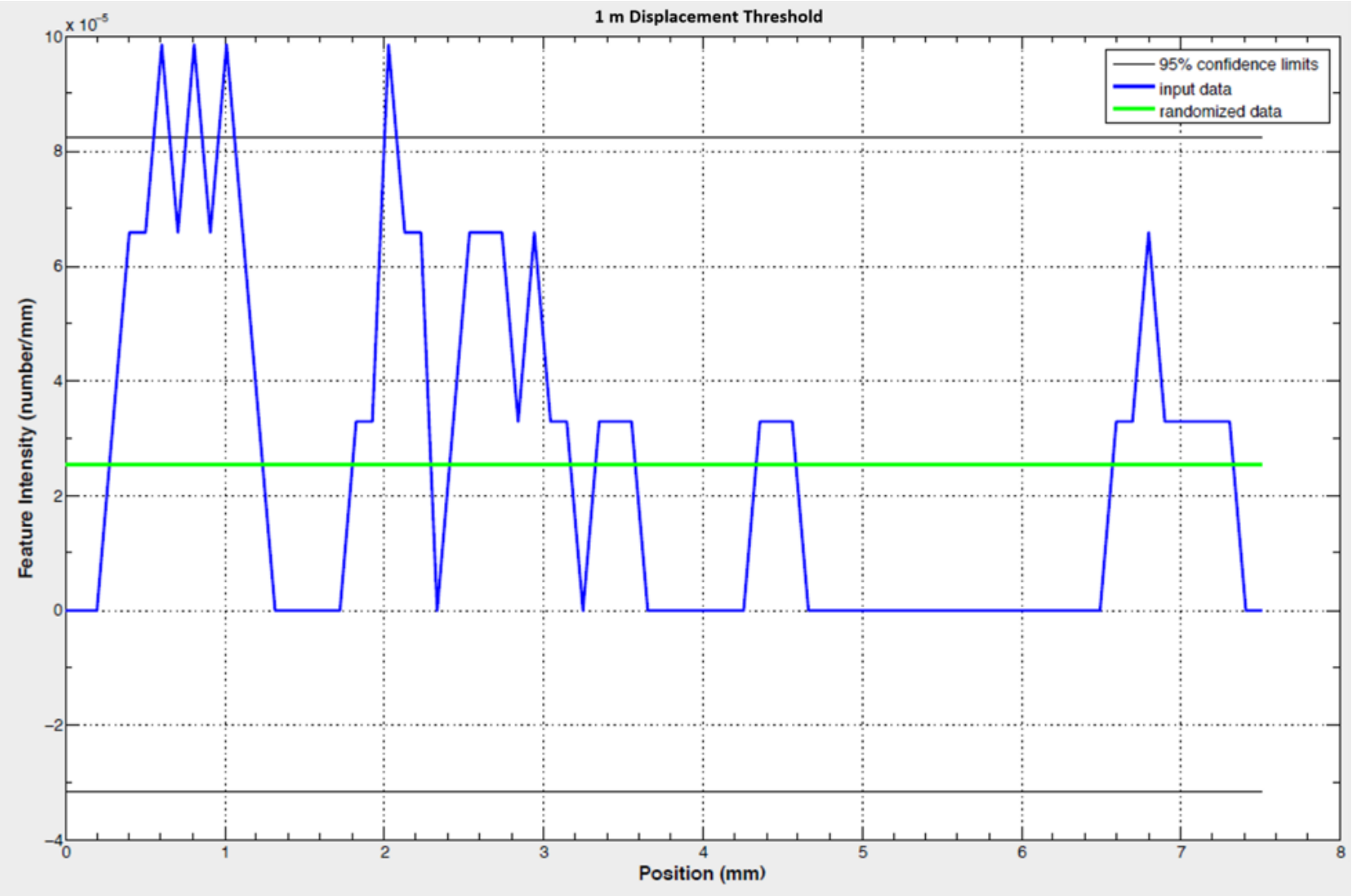

Figure 21: Intensity plot of the 1 meter threshold dataset comparing scanline position in millimeters (X-Axis) to the fracture intensity (Y-Axis). The plot also contains a windowing value of 1.

NCC of scanline A shows multiple positive anomalies but only two ranges of length scale, approximately 18 – 23 m and approximately 42 – 46 m, in the NCC log-log plot, exceed the 2σ confidence limit and are therefore significant (Figure 22 A, B). These indicate that faults exhibit a characteristic regular spacing of approximately 20 meters. Unlike higher resolution datasets, the NCC log-log plot lacks a plateau shape and instead decreases for smaller length scales. Therefore, clustering in the higher resolution datasets is absent for faults having displacement ≥ 1 m. These faults instead show regular spacing of approximately 20 meters. The regular spacing of 20 meters represents spacing from one feature to the next whereas the second peak at approximately 40 meters reinforces the 20-meter spacing by being approximately double the nearest neighbor spacing. These characteristics define a pattern of regularly spaced faults for the 1 m displacement threshold scanline.

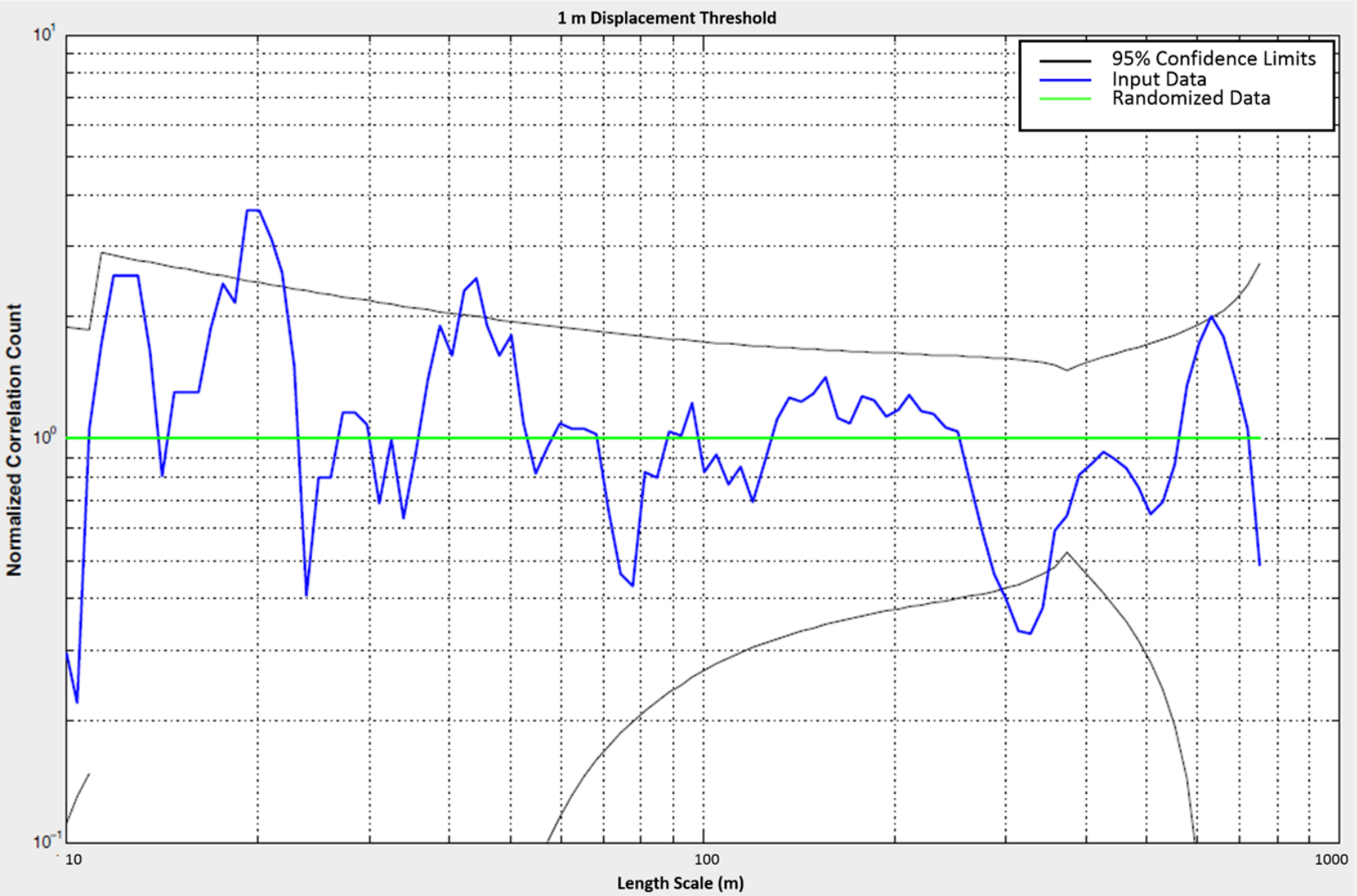

Figure 22A: NCC log-log plot of the 1 meter (1 m) threshold dataset comparing length scales in millimeters (X-Axis) to the normalized correlation count (Y-Axis).

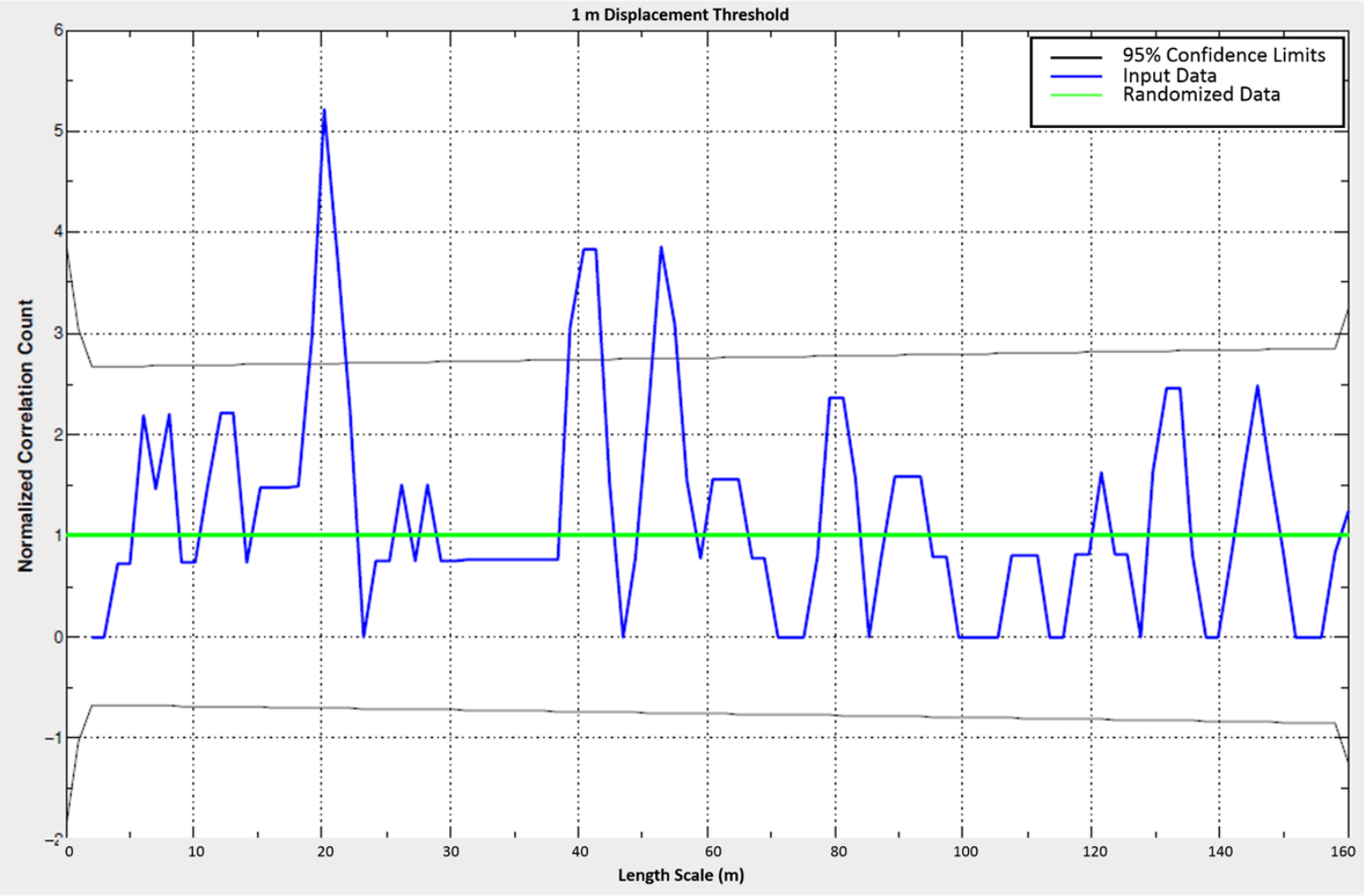

Figure 22B: Linear-linear plot of the 1 meter (1 m) threshold dataset comparing length scales in millimeters (X-Axis) to the normalized correlation count (Y-Axis).

Section 7. Discussion

Size distribution analysis of normal faults in A-Bomb Canyon show consistent scaling defined by a power-law for fault displacements across more than four orders of magnitude (0.001 m displacement up to ~100 m displacement; Figure 14). Investigating the displacement distribution of each scanline with thresholds at four different orders of magnitude demonstrates this scaling.

NCC analyses of normal faults at all scales in A-Bomb Canyon show a complementary similarity. The three smallest displacement thresholds (0.001 m, 0.01 m, 0.1 m) show clustering in the form of a plateau-and-trough pattern. The plateau portion of the pattern exists at the shorter length scales and the trough pattern exists towards the longer length scales. The highest displacement threshold data (1 m) lack the clustering pattern but instead indicates regular spacing of the largest faults.

MODELS OF FAULT GROWTH

Two competing fault growth models were compared to evaluate how faults became localized in A-Bomb Canyon. Nicol et al. (2016) postulated fault growth by fault tip splays, which tends to be consistent with a constant fault length growth model. Alternatively, Cladouhos and Marrett (1996) presented the idea that a combination of fault growth and fault linkage produces a power-law distribution of fault lengths from initially randomly spatially distributed flaws.

The constant fault length growth model postulates that faults experience two phases: an initial rapid fault propagation stage followed by a longer displacement accumulation stage (Nicol et al., 2016). The initial fault propagation stage lasts until fault saturation has been reached, during which all faults mechanically interact with one another. Then a stage of displacement dominated growth occurs where there is limited fault propagation and fault termination, all while displacement accumulates through further fault interaction. The constant length growth model was found to have possible applications across five orders of magnitude from regional (e.g. lengths of 1-50 km and displacements of 0.1-3 km: Walsh et al. 2002) to outcrop-scale (e.g. lengths of 0.4-200 m

and displacements of 0.002-3 m) for faults with significant components of dip slip (Nicol et al. 2016).

Faulted regions are finite in size, like A-Bomb Canyon, because of stratigraphic or structural boundaries, and because of this finite-size fault length data from most areas may show rollover on a log-log plot (Cladouhos and Marrett (1996). The power-law distribution model postulates that progressive linkage produces a steeper trend or rollover. A rollover is a change in the slope of the plot from a non-trivial slope to a slope that progressively approaches zero at long faults. Rollover has been attributed to sampling artifacts (Marrett and Allmendinger, 1992). More recently, Cladouhos and Marrett (1996) suggested instead that rollover at longer fault lengths may occur because longer faults are unable to grow at rates sufficient to maintain a power-law distribution defined by shorter faults. They concluded that linkage is a very effective process for creating a power-law length distribution from a population that initially does not contain one.

POWER-LAW PATTERNS OF DISPLACEMENT DISTRIBUTION

The distribution of fault displacements for faults meeting four different displacement thresholds exhibit fractal behavior. All four displacement thresholds show a negatively sloping power-law scaling, with exponents within the range of -0.6 and -0.9. This small difference in range permits the conclusion that all of the faults exhibit similar scaling, consistent with other similarities in age, kinematics and fault orientations. The power-law distribution observed for the faults in A-Bomb Canyon has a slightly larger range of power-law exponents than those observed for opening mode fracture (Hooker et al., 2014), but the exponents are similar. The observation of power-law scaling of normal faults in A-Bomb Canyon is more consistent with the linkage fault growth model (Cladouhos and Marrett, 1996) as opposed to the constant length growth model (Nicol et al. 2016), which does not exhibit power-law scaling.

REGULAR FAULT SPACING PATTERNS AND SPATIAL CORRELATION

Clustering is indicated in CorrCount analyses by a plateau or power-law portion in NCC graphs for the shortest length scales, until the NCC descends below a value of 1 at a finite length scale corresponding to cluster width (Figure 8B, D). In contrast, periodicity of individual fractures in CorrCount shows NCC < 1 for the shortest length scales and a systematic wave pattern as the length scale increases (Figure 8E). When a systematic wave pattern is present in a linear graph of NCC, it can be concluded that there is no evidence of clustering, but there is evidence of periodicity or regular spacing of individual features, such as is seen in the > 1 meter displacement threshold NCC analysis.

The largest faults show regular spacing of approximately 20 meters between features without clustering. The NCC plot (Figure 22 A, B) displays a wave pattern with an isolated peak at 20 meters (and an overtone at double this length) instead of a plateau-and-trough or power-law pattern indicative of clustering. What controls this spacing?

The Chapin Wash Formation is distinctly layered sandstone, siltstone and tuff with different mechanical properties that may control fault localization. Mechanical properties of rock layers strongly influence nucleation points, failure mode, fault geometry and propagation rates that influence displacement and other fault-zone deformation processes (Ferrill et al., 2016). Without an understanding of the mechanical properties, it is not possible to know which, if any, had a controlling influence on the faulting. Earlier reported variation in fault geometry in the Chapin Wash Formation (Laubach et al., 1992) could provide some mechanical information, such as which stratigraphic layers are more prone to faulting than others. This study shows that there is a pattern of fault spacing and literature indicates that this pattern could be controlled by one or more factors, including the mechanical properties of intraformational layers.

PLATEAU-AND-TROUGH PATTERNS OF SPATIAL CORRELATION

Clustering is indicated in CorrCount analysis by seeing a plateau or power-law portion of the NCC graph for the shortest length scales until the NCC value descends below a value of 1 at a finite length scale corresponding to cluster width (Figure 8B).

NCC plots for the 0.001 m, 0.01 m and the 0.1 m displacement thresholds all exhibit a plateau-and-trough pattern, indicating that fault with these thresholds clusters at definable widths.

The spatial correlation of normal faults for the 0.001 meter displacement threshold exhibit a plateau pattern at length scales from 0.02-0.9 m (Figure 16 A, B). For the displacement threshold of 0.01 meter, there is a plateau pattern on length scales from 0.01-14 m (Figure 18 A, B). Finally, for the displacement threshold of 0.1 meter, a plateau pattern exists on length scales from 0.1-15 meters (Figure 20 A, B). In contrast, when analyses are restricted to the 1 meter displacement threshold, the plateau pattern disappears and is replaced by a pattern that indicates regular spacing of about 20 meters (Figure 22 A, B). The plateau patterns and the associated troughs indicate inherited/imposed clusters with varying widths which can be detected in the NCC analyses where the data crosses the value of one. For the 0.001 meter, 0.01 meter, and 0.1 meter displacement thresholds there is evidence from NCC analyses of cluster widths of approximately 1 meter, approximately 14 meters, and approximately 15 meters respectively. The latter two cluster widths are very similar and approximate the distance between Faults B and C.

The results from the NCC analyses indicate that the inherited/imposed clusters correspond with the smaller displacement threshold (all <1 meter data) faults whereas the larger threshold displacement faults (>1 meter) exhibit a regular spacing of features but lack evidence of clustering. A simple explanation for this outcome is the possibility that between the larger regularly spaced faults are domains containing clusters of smaller displacements faults. Relay ramps between larger displacement faults, connecting the footwall to the hanging wall of the faults and transferring displacement between the faults, allow for the transfer of displacement along strike between large displacement faults (Peacock and Sanderson, 1991). Fault displacement, which is discontinuous deformation, combined with tilting of layers within a relay ramp can be approximately constant across faults. This continuous deformation in the form of relay ramp tilting between soft-linked faults may explain the clustering seen in the smaller displacement

faults found to be clustered with widths smaller than the regular spacing of the larger displacement faults in this study.

FAULTS IN MAP VIEW

Faults in A-Bomb Canyon follow a power-law distribution of fault displacements as predicted by the linkage-dominated fault growth model (Cladouhos and Marrett, 1996). Due to the similarity of power-law distribution model and the power-law distributions in A-Bomb Canyon, it can be hypothesized that the power-law distribution model is the better fitting of the fault growth models in this instance. There is some evidence that the two-phase model presented by Nicol et al. (2016) may be applicable as well due to the presence of the fault tip splays seen on some of the faults in A-Bomb Canyon, but the faults appear to agree more closely with the power-law distribution model than the two-phase fault growth model. The findings from the spatial arrangement are more appropriate for the linkage-dominated fault growth model. This is best seen in the centimeter displacement threshold spatial arrangement, where the most significant positive anomaly falls between Faults B and C (Figure 18A, B). This supports the idea that there is a relay ramp between the larger faults and the associated deformation is creating the cluster of smaller faults within the ramp area.

Section 8: Conclusions

In this study, normal faults along two scanlines of different lengths were organized into four datasets by the order of magnitude of fault displacement. This study was designed to gain an understanding of the size distribution and spatial arrangement of faults across four orders of magnitude of displacement.

Size Distribution of Fault Displacements

Data across four orders of displacement magnitude exhibit a power-law scaling. All power-law scalings are characterized by negative power-law exponents, ranging from -0.614 to -0.866. This similarity allows for the determination that normal faults in A-Bomb Canyon and the surrounding area all follow a scaling described by power-laws. Given my research is another fracture size distribution dataset on a differing scale than the ones found in previous work (Marrett et al., 1999), this evidence of a strong linear trend following a power-law distribution supports the determination in previous work that displacements of brittle fractures, in this case normal faults, can be characterized as a single fractal across a wide range of scales. The uniformity of negative power-law exponents for these normal faults is very similar to that seen in other work on fractures, most notably opening-mode fractures of all different sizes (Hooker et al., 2014). Further work should include a larger displacement threshold to understand whether power-law scaling extends to yet higher order-of-magnitude displacements. Fault data with a < 1 mm threshold may also provide an understanding of whether power-law scaling extends to a lower displacement threshold.

Spatial Arrangement

Correlation Count analysis shows that the largest displacement faults (> 1 meter displacement) exhibit regular spacing of approximately 20 meters. Inherited/imposed clustering is exhibited by fault datasets with thresholds of 0.001 m, 0.01 m, and 0.1 m. Cluster widths are approximately 1 meter for the 0.001 m displacement threshold faults, approximately 14 meters for the 0.01 meter displacement threshold faults and

approximately 15 meters for the 0.1 meter displacement threshold faults. No clustering is exhibited by the > 1 meter displacement faults.

Appendix A

Raw Normal Fault Scanline Data

Greater than 1 Meter Displacement Scanline. Raw spacing was collected with a tape measure on the topographic surface. The plunge of the scanline on the surface was also recorded in order to correct the raw spacing data and provide a more accurate corrected spacing. Some faults are listed multiple times as their fault surfaces allowed for multiple measurements of strike and dip.

Fault Number	Fault Name	Displacement (m)	Fault Strike (°)	Fault Dip (°)	Spacing (m)	Corrected Spacing (m)
1	A	Unknown	313	43	42.3672	41.846
1	A	Unknown	314	49	-	-
1	A	Unknown	321	51	-	-
1	A	Unknown	323	39	-	-
1	A	Unknown	328	43	-	-
1	A	Unknown	328	46	-	-
1	A	Unknown	316	41	-	-
2	A1	1.304	140	65	19.324	19.324
3	A2	1.558	150	45	15.636	15.636
4	A3	2.469	305	41	4.602	4.602
5	A4	1.541	141	69	11.46	11.376
6	A5	Unknown	322	56	9.053	9.053
7	A6	0.84	140	71	19.568	19.568
8	A7	7.065	321	56	84.369	81.548
8	A7	7.065	318	37	-	-
8	A7	7.065	324	33	-	-
9	A8	1.11	130	78	12.009	12.009
9	A8	1.11	120	64	-	-
10	A9	1.27	334	28	6.37	6.37
10	A9	1.27	317	25	-	-

11	A10	2.66	322	37	40.569	40.513
12	B	31.5	309	52	6.218	6.218
13	C	1.5	303	72	20.665	20.511
13	C	1.5	297	79	-	-
13	C	1.5	298	68	-	-
13	C	1.5	299	79	-	-
13	C	1.5	311	83	-	-
13	C	1.5	297	79	-	-
13	C	1.5	290	52	-	-
14	D	27.18	135	82	18.806	18.806
14	D	27.18	118	74	-	-
14	D	27.18	134	77	-	-
14	D	27.18	128	76	-	-
15	D1	1.463	280	61	45.507	45.507
15	D1	1.463	287	71	-	-
15	D1	1.463	290	65	-	-
16	E	8.5	285	57	103.053	100.709
16	E	8.5	283	54	-	-
16	E	8.5	293	59	-	-
16	E	8.5	289	52	-	-
17	E1	4.1	337	72	222.87	220.751
17	E1	4.1	345	67	-	-
18	E2	22.5	305	71	12.527	12.527
19	E3	4.85	310	72	37.429	37.429
Scanline End					32.431	31.722

Appendix B

> 1 Centimeter Displacement Scanline Raw Data

Fault Number	Displacement (cm)	Spacing (m)	Fault Dip Direction
1	23	0.04	NE
2	3.4	0.07	SW
3	1	0.025	NE
4	2.9	0.233	SW
5	4.6	0.231	SW
6	4.5	0.015	NE
7	2	0.207	SW
8	9.5	0.11	NE
9	2.1	0.565	SW
10	18	0.198	NE
11	2.4	0.38	SW
12	3	0.64	NE
13	7.5	0.17	NE
14	48	0.11	NE
15	10	0.13	NE
16	4.8	0.24	NE
17	6.5	0.31	NE
18	56	0.19	NE
19	2.7	0.496	NE
20	3.1	0.062	SW
21	1.9	0.33	NE
22	1.3	0.64	SW
23	16	0.86	NE
24	4	0.73	NE
25	51	0.52	NE
26	1500	0.065	NE
27	8.5	0.18	NE
28	9	0.078	NE
29	1.4	0.027	NE
30	1.9	0.038	NE
31	6.3	0.025	NE
32	10	0.018	NE
33	2.5	0.025	SW
34	7.5	0.176	NE
35	1.7	0.123	NE

36	2.1	0.061	NE
37	2.9	0.053	SW
38	1.1	0.011	SW
39	3.7	0.11	SW
40	3.4	0.143	SW
41	2.8	0.156	NE
42	4.8	0.19	NE
43	5.8	0.157	SW
44	1.3	1.485	SW
45	16	0.018	NE
46	2.2	0.023	NE
47	2.6	0.066	NE
48	1.3	0.111	NE
49	1.2	0.011	SW
50	2.1	0.099	NE
51	2.9	0.038	NE
52	1.4	0.016	NE
53	2.4	0.053	NE
54	4.4	0.13	NE
55	6.7	0.16	NE
56	3.8	0.068	NE
57	6.4	0.078	NE
58	2.9	0.032	SW
59	1.7	0.02	NE
60	1.1	0.13	NE
61	1	0.085	SW
62	3.6	0.12	SW
63	13	0.062	NE
64	2.2	0.05	NE
65	1.8	0.061	NE
66	1.8	0.011	SW
67	1.1	0.047	SW
68	110	0.024	NE
69	1.1	0.1	NE
70	1	0.023	NE
71	3.1	0.073	NE
72	2.3	0.06	NE
73	1	0.025	NE
74	2.1	0.066	NE
75	1.5	0.044	NE

76	1.6	0.042	SW
77	1.3	0.032	SW
78	1.1	0.13	NE
79	1.9	0.048	NE
80	4.8	0.016	SW
81	1	0.082	NE
82	5.6	0.075	NE
83	1.2	0.26	NE
84	4.2	0.016	NE
85	1.5	0.056	NE
86	1.4	0.078	SW
87	1.7	0.024	SW
88	2.1	0.022	SW
89	1.5	0.048	NE
90	3.3	0.008	NE
91	2.6	0.01	NE
92	1.3	0.067	NE
93	1	0.013	NE
94	11	0.013	NE
95	3.4	0.032	NE
96	3.6	0.091	NE
97	1.8	0.018	NE
98	2.8	0.17	NE
99	4.1	0.15	NE
100	1.9	0.027	NE
101	1.8	0.11	NE
102	14	0.022	NE
103	1.5	0.021	NE
104	2.9	0.15	NE
105	8.3	0.04	SW
106	2.1	0.003	SW
107	1.5	0.048	NE
108	1.3	0.039	NE
109	1.4	0.051	NE
110	1	0.026	NE
111	1.7	0.061	NE
112	13	0.046	NE
113	11	0.032	NE
114	1.4	0.018	NE
115	1.7	0.15	NE

116	1.8	0.11	NE
117	3.1	0.078	NE
118	1	0.062	NE
119	21	0.11	NE
120	2.6	0.2	NE
121	1.3	0.069	NE
122	18	0.028	NE
123	2.7	0.077	NE
124	2	0.01	NE
125	2.4	0.15	NE
126	3.8	0.019	NE
127	49	0.018	NE
128	4.5	0.081	NE
129	2.2	0.072	NE
130	5.8	0.095	NE
131	1.1	0.054	NE
132	2.6	0.17	NE
133	1.1	0.18	NE
134	1.2	0.029	NE
135	1.6	0.032	NE
136	1.8	0.24	NE
137	5.3	0.6	NE
138	1.2	0.036	NE
139	39	0.12	NE
140	1.6	0.13	SW
141	16	0.37	SW
142	2.2	0.058	NE
143	2.5	0.13	NE
144	1.6	0.29	NE
145	16	0.008	NE
146	1	0.017	NE
147	1.2	0.18	NE
148	1.4	0.083	NE
149	1	0.026	NE
150	1	0.14	NE
151	2.3	0.048	NE
152	2	0.028	SW
153	2.1	0.02	NE
154	2.7	0.005	SW
155	1.8	0.015	NE

156	1.5	0.007	SW
157	8.5	0.029	NE
158	6.5	0.15	SW
159	3	0.067	NE
160	2.7	0.09	NE
161	1.1	0.1	NE
162	1	0.075	NE
163	9.5	0.051	SW
164	15	0.012	SW
165	2.8	0.023	SW
166	2.4	0.02	NE
167	3.1	0.031	NE
168	1.2	0.11	SW
169	1.5	0.15	NE
170	1.3	0.072	NE
171	7.9	0.34	NE
172	4.9	0.017	NE
173	1.1	0.06	NE
174	1	0.4	NE
175	2.3	0.028	NE
176	2.7	0.075	NE
177	1.6	0.12	NE
178	86	0.33	SW
179	3.3	0.032	NE
180	4.2	0.014	SW
181	1.4	0.125	SW
182	7.4	0.115	NE
183	4.7	0.012	NE
184	2.2	0.027	NE
185	3.8	0.036	NE
186	1.5	0.13	NE
187	5.1	0.135	NE
188	4	0.008	SW
189	1.3	0.015	SW
190	3.6	0.11	NE
191	1	0.23	NE
192	1.1	0.23	NE
193	8.5	0.125	SW
194	2.2	0.015	NE
195	1	0.007	NE

196	1.3	0.12	SW
197	1.1	0.11	NE
198	1	0.12	NE
199	3.8	0.21	SW
200	1.4	0.034	SW
201	6.8	0.23	NE
202	1.9	0.22	NE
203	3.4	0.42	NE
204	1.2	0.027	NE
205	12	0.22	NE
206	14	0.018	SW
207	2.4	0.037	SW
208	2.9	0.046	NE
209	1.5	0.11	SW
210	3.2	0.076	NE
211	1.4	0.088	NE
212	1.8	0.21	SW
213	32	0.007	NE
214	2.9	0.14	NE
215	1.1	0.064	SW
216	1.6	0.235	SW
217	53	0.22	NE
218	4.8	0.021	NE
219	1.6	0.034	NE
220	1	0.013	NE
221	3.3	0.031	NE
222	1	0.079	NE
223	1.8	0.11	NE
224	11	0.065	NE
225	1.5	0.01	SW
226	9	0.31	NE
227	1.1	0.085	NE
228	1	0.032	SW
229	3.2	0.13	NE
230	1.8	0.125	NE
231	3.2	0.089	NE
232	1.7	0.36	NE
233	11.5	0.12	NE
234	39	0.091	NE
235	1.9	0.039	NE

236	430	0.84	NE
237	17	0.093	NE
238	4	0.075	NE
239	1.3	0.29	NE
240	3.4	0.5	NE
241	27	0.7	SW
242	3.9	0.19	NE
243	18	0.59	NE
244	7.5	0.14	NE
245	3.2	0.088	NE
246	1	0.7	NE
247	1.2	0.073	NE
248	1	0.1	NE
249	8.5	0.061	SW
250	1	0.11	SW
251	2.8	0.19	NE
252	5.2	0.8	NE
253	2.1	4.2	SW
254	10	2.7	SW
255	1	0.12	NE
256	1.7	0.9	NE
257	2.5	2.6	NE
258	2.2	1.85	NE
259	1	0.062	NE
260	1.9	0.54	NE
261	3.1	0.061	NE
262	19	0.86	NE
263	1.1	3.35	NE
264	1.5	0.073	SW
265	4.5	0.28	SW
266	3.8	0.31	SW
267	5.5	1.15	SW
268	6.5	3	SW
269	4.1	0.83	SW
270	1.1	1.02	SW
271	4.2	3.9	SW
272	660	0.12	SW
273	1.2	0.085	SW
274	1.1	0.1	SW
275	8	0.42	SW

276	2.1	0.23	NE
277	2.6	0.26	SW
278	3.4	0.095	NE
279	1.3	1.2	NE
280	2.4	0.041	SW
281	1	0.8	NE
282	1.1	0.33	NE
283	5.2	1.1	NE
284	6.3	0.13	NE
285	1.1	0.036	NE
286	1.3	0.069	NE
287	4.2	0.089	NE
288	1.2	0.21	NE
289	320	0.035	NE
290	1.8	9.2	NE
291	75	0.41	NE
292	5.6	0.59	SW
293	8.6	0.29	SW
294	1.6	0.38	SW
295	1.4	0.042	SW
296	4.7	0.43	NE
297	7.7	0.19	NE
298	2.2	0.15	SW
299	14	0.1	SW
300	1	0.2	NE
301	1.7	0.013	NE
302	10.5	0.068	SW
303	1.5	0.087	SW
304	1.1	0.038	NE
305	4.9	0.012	NE
306	2.8	0.032	NE
307	1.1	0.014	SW
308	2.2	0.15	SW
309	1.3	0.067	NE
310	1.1	0.011	SW
311	6.9	0.059	SW
312	1.2	0.026	NE
313	1	0.012	NE
314	1.2	0.078	NE
315	20	0.29	NE

316	2	0.015	NE
317	1	0.2	SW
318	1.3	0.31	SW
319	1.6	0.071	SW
320	1.1	0.19	NE
321	1.2	0.33	SW
322	1	0.49	SW
323	1.4	0.013	NE
324	4.5	0.15	NE
325	1.1	5.1	NE
326	2.2	0.059	NE
327	1.2	0.067	SW
328	1.4	0.68	NE
329	7.3	0.51	SW
330	1.1	0.044	SW
331	1.6	0.16	NE
332	1.1	0.018	SW
333	1	0.52	SW
334	2.3	0.46	SW
335	14	0.67	SW
336	6.8	1.25	NE
337	7.2	0.04	SW
338	3.9	0.125	SW
339	3.6	0.155	NE
340	1.3	0.022	NE
341	1	0.14	NE
342	3.2	0.52	NE
343	1.4	0.24	NE
344	1.2	0.62	SW
345	42	0.095	SW
346	1.8	0.13	NE
347	1	0.045	NE
348	4.2	0.49	NE
349	1.2	0.011	NE
350	2.7	0.64	NE
351	1.1	1.45	NE
352	5.6	0.44	SW
353	9.1	0.28	SW
354	1.5	2.3	SW
355	2.5	0.73	NE

356	19	0.085	SW
357	1.7	0.39	SW
358	36	0.45	SW
359	5.8	0.135	SW
360	19	0.4	SW
361	4.8	0.61	SW
362	1.2	0.058	SW
363	7.2	0.23	SW
364	4.4	1.27	SW
365	1.2	0.46	SW
366	33	0.11	SW
367	5.8	0.16	SW
368	8.6	0.115	NE
369	1.2	0.21	SW
370	1.2	0.065	NE
371	1.6	0.056	SW
372	10.5	0.098	SW
373	3.8	0.063	SW
374	2.8	0.092	SW
375	1	0.26	SW
376	6.2	0.17	SW
377	1.3	1.25	SW
378	6.7	0.29	SW
379	2.3	0.17	SW
380	7	0.06	SW
381	20	0.031	SW
382	1.2	0.23	SW
383	1.1	2.1	SW
384	3.4	0.057	SW
385	1.3	0.49	SW
386	2.5	1.75	NE
387	67	0.76	SW
388	9.7	0.058	SW
389	4.4	0.036	SW
390	3.7	0.32	SW
391	1.7	0.032	SW
392	1.3	0.028	SW
393	4.2	0.2	SW
394	39	0.105	NE
395	44	0.125	NE

396	1.1	0.018	SW
397	1.2	0.018	SW
398	1	0.016	SW
399	1.1	0.023	SW
400	2.3	0.069	SW
401	1.5	0.46	NE
402	1.8	0.53	SW
403	3.8	0.29	NE
404	1.1	0.4	SW
405	31	0.15	NE
406	2.1	0.25	SW
407	1	0.73	NE
408	1.2	0.89	NE
409	8.6	0.24	SW
410	3.2	0.28	SW
411	1.1	0.024	NE
412	3.3	0.83	NE
413	16.5	0.38	SW
414	1.1	0.31	NE
415	1.9	1.14	SW
416	1.3	0.79	NE
417	1.2	0.035	SW
418	4.1	0.074	SW
419	14	0.35	SW
420	29	0.49	SW
421	1.6	0.74	NE
422	39	0.033	NE
423	2.7	0.125	NE
424	1.7	0.145	SW
425	1.1	0.49	SW
426	1.9	0.64	SW
427	2.7	0.034	SW
428	12.5	0.54	SW
429	1.1	0.072	SW
430	1.7	0.6	SW
431	1	0.066	SW
432	13		SW

Appendix C

> 1 Millimeter Displacement Scanline Raw Data

Fault Number	Displacement (cm)	Spacing (cm)	Fault Dip Direction
1	23	4	NE
2	3.4	3.5	SW
3	0.6	3.5	NE
4	1	2.5	NE
5	2.9	9.2	SW
6	0.1	4.6	SW
7	0.6	9.5	SW
8	4.6	7.4	SW
9	0.8	13.5	SW
10	0.8	2.2	NE
11	4.5	1.5	NE
12	2	12	SW
13	0.5	4	SW
14	0.6	4.7	SW
15	9.5	11	NE
16	2.1	11	SW
17	0.2	14.5	SW
18	0.6	31	SW
19	18	7.2	NE
20	0.4	4.5	SW
21	0.3	8.1	SW
22	2.4	38	SW
23	3	64	NE
24	7.5	17	NE
25	48	11	NE
26	10	13	NE
27	4.8	24	NE
28	6.5	6	NE
29	0.3	25	NE
30	56	19	NE
31	2.7	7.6	NE
32	0.8	42	NE
33	3.1	6.2	SW
34	1.9	33	NE
35	1.3	64	SW

36	16	86	NE
37	4	17	NE
38	0.8	28	SW
39	0.6	28	NE
40	51	52	NE
41	1500	6.5	NE
42	8.5	18	NE
43	9	4.3	NE
44	0.5	3.5	NE
45	1.4	2.7	NE
46	1.9	3.8	NE
47	6.3	2.5	NE
48	10	1.8	NE
49	2.5	2.5	SW
50	7.5	0.9	NE
51	0.7	2.1	SW
52	0.7	13	SW
53	0.7	1.6	NE
54	1.7	2.4	NE
55	0.5	2.6	SW
56	0.6	1.5	NE
57	0.3	5.1	NE
58	0.5	0.7	NE
59	2.1	6.1	NE
60	2.9	1.3	SW
61	0.4	3.4	NE
62	0.9	0.6	SW
63	1.1	1.1	SW
64	3.7	5.9	SW
65	0.3	1.8	NE
66	0.8	3.3	NE
67	3.4	3.1	SW
68	0.5	6.4	NE
69	0.9	4.8	NE
70	2.8	4.4	NE
71	0.2	4.4	NE
72	0.3	1.4	NE
73	0.2	1.7	NE
74	0.2	3.7	NE
75	4.8	19	NE

76	5.8	0.7	SW
77	0.6	3	SW
78	0.3	2.3	SW
79	0.3	3.4	SW
80	0.5	0.6	NE
81	0.7	0.4	NE
82	0.7	4.6	NE
83	0.4	0.7	SW
84	1.3	49	SW
85	0.1	5.5	NE
86	0.2	94	SW
87	16	1.8	NE
88	2.2	2.3	NE
89	2.6	2.1	NE
90	0.4	1.8	NE
91	0.6	2.2	NE
92	0.7	0.5	NE
93	1.3	5.2	NE
94	0.5	1.2	NE
95	0.8	2.7	NE
96	0.4	0.6	NE
97	0.7	1.4	SW
98	1.2	1.1	SW
99	2.1	3.6	NE
100	0.8	6.3	NE
101	2.9	3.8	NE
102	1.4	1.6	NE
103	2.4	5.3	NE
104	4.4	13	NE
105	6.7	16	NE
106	3.8	6.8	NE
107	6.4	1.9	NE
108	0.4	1.7	NE
109	0.5	2	NE
110	0.9	2.2	NE
111	2.9	3.2	SW
112	1.7	2	NE
113	1.1	13	NE
114	1	8.5	SW
115	3.6	12	SW

116	13	6.2	NE
117	2.2	5	NE
118	1.8	6.1	NE
119	1.8	1.1	SW
120	1.1	2.4	SW
121	0.6	2.3	NE

Appendix D

Raw fault kinematic data collected along A-Bomb Canyon scanlines

Fault Strike (°)	Fault Dip (°)	Lineation Trend (°)	Lineation Plunge (°)	Sense of Slip
154	68	251	63	Normal
341	61	64	62	Normal
310	47	41	46	Normal
344	38	72	41	Normal
334	29	71	30	Normal
147	76	299	58	Normal
171	32	253	31	Normal
172	32	250	32	Normal
163	44	289	38	Normal
341	43	104	38	Normal
143	52	203	48	Normal
302	49	34	49	Normal
306	50	67	46	Normal
305	48	51	47	Normal
303	62	39	62	Normal
321	48	29	46	Normal
294	57	41	56	Normal
313	57	56	56	Normal
322	18	57	18	Normal
346	75	49	73	Normal
314	52	60	51	Normal
358	52	36	38	Normal
332	48	67	48	Normal
003	48	34	30	Normal
159	66	228	65	Normal
161	79	240	79	Normal
313	43	27	43	Normal
314	49	33	49	Normal
328	43	33	44	Normal
309	52	36	51	Normal
311	83	65	84	Normal
297	79	9	80	Normal
290	52	14	56	Normal

Appendix E

GPS Data for Scanlines B, C, D Start Point and Endpoint and GPS Data for Scanline A > Start Point and Endpoint and Fault Locations

Label	Latitude	Longitude
High-Resolution "Scan 1a"	34°10'34.69"N	113°40'18.32"W
High-Resolution "Scan 1b"	34°10'35.08"N	113°40'19.81"W
High-Resolution "Scan 2a"	34°10'42.29"N	113°40'28.47"W
High-Resolution "Scan 2b"	34°10'42.13"N	113°40'32.80"W
Low-Resolution Scanline Start	34°10'35.70"N	113°40'8.40"W
A	34°10'34.70"N	113°40'9.00"W
A1	34°10'34.30"N	113°40'10.10"W
A2	34°10'34.30"N	113°40'10.50"W
A3	34°10'35.20"N	113°40'11.50"W
A4	34°10'35.00"N	113°40'11.60"W
A5	34°10'34.40"N	113°40'11.70"W
A7	34°10'33.50"N	113°40'14.80"W
A8	34°10'33.10"N	113°40'14.90"W
A9	34°10'33.20"N	113°40'16.00"W
B	34°10'33.60"N	113°40'17.40"W
C	34°10'40.10"N	113°40'26.20"W
D	34°10'39.20"N	113°40'25.50"W
D1	34°10'37.80"N	113°40'25.60"W
E	34°10'34.50"N	113°40'25.10"W
E1	34°10'27.50"N	113°40'27.60"W
E2	34°10'26.90"N	113°40'27.80"W
E3	34°10'32.07"N	113°40'18.97"W
Low-Resolution Scanline End	34°10'25.00"N	113°40'29.00"W

References

Allmendinger, R.W., Marrett, R.A., and Cladouhos, T., 1992, FaultKin Version 3.25, computer program and user's manual, 26 p.

Armstrong, R.L., 1982, Cordilleran metamorphic core complexes - from Arizona to southern Canada: Annual Review of Earth and Planetary Sciences. v. 10, p. 129-154.

Barton, C.C, 1995, Fractal analysis of scaling and spatial clustering of fractures, in Barton, C.C., and La Pointe, P.R., eds., Fractals in the Earth Sciences, p. 141-178.

Bonnet, E., Bour, O., Odling, N.E., Davy, P., Main, I., Cowie, P., and Berkowitz, B., 2001, Scaling of fracture systems in geological media: Reviews of Geophysics, v. 39, p. 347-383.

Bour, O., and Davy, P., 1999, Clustering and size distributions of fault patterns: theory and measurements: Geophysical Research Letters, v. 26, no. 13, p. 2001-2004.

Bryant, B. H., 1995, Geologic map, cross sections, isotopic dates, and mineral deposits of the Alamo Lake 30'x 60' Quadrangle, west-central Arizona: U.S. Geological Survey Open-File Report 92-311, Series no. 2489, scale 1:100,000.

Carter, T.J., Kohn, B.P., Foster, D.A., and Gleadow, A. J., 2004, How the Harcuvar Mountains metamorphic core complex became cool: Evidence from apatite (U-Th)/He thermochronometry: Geology, v. 32, p. 985-988.

Cladouhos, T.T., and Marrett, R., 1996, Are fault growth and linkage models consistent with power-law distributions of fault lengths?: Journal of Structural Geology, v. 18, p. 281-293.

Coney, P.J., and Harms, T.A., 1984, Cordilleran metamorphic core complexes: Cenozoic extensional relics of Mesozoic compression: Geology, v. 12, p. 550-554.

Du Bernard, X., Labaume, P., Darcel, C., Davy, P., and Bour, O., 2002, Cataclastic slip band distribution in normal fault damage zones, Nubian sandstones, Suez rift: Journal of Geophysical Research: Solid Earth, v. 107, p. ETG 6-1 – ETG 6-12.

Ferrill, D.A., Morris, A.P., McGinnis, R.N., Smart, K.J., Wigginton, S.S., and Hill, N.J., 2017, Mechanical stratigraphy and normal faulting: Journal of Structural Geology, v. 94, p. 275-302.

Foster, D.A., Gleadow, A.J., Reynolds, S.J., and Fitzgerald, P.G., 1993, Denudation of metamorphic core complexes and the reconstruction of the transition zone, west central Arizona: Constraints from apatite fission track thermochronology: Journal of Geophysical Research: Solid Earth, 98, p. 2167-2185.

Gale, J.F., Laubach, S.E., Olson, J.E., Eichhubl, P., and Fall, A., 2014, Natural fractures in shale: A review and new observations: American Association of Petroleum Geologists Bulletin, Special Issue on Faulting and Fracturing in Shale and Self-Sourced Reservoirs, v. 98, p. 2165-2216.

Gale, J., Ukar, E., Elliott, S.J., and Wang, Q., 2015, Bedding-Parallel Fractures in Shales: characterization, prediction and importance (abs): AAPG Annual Meeting, Denver, Colorado.

Gehrels, G.E., and Spencer, J.E., 1990, Geologic excursions through the Sonoran Desert Region, Arizona and Sonora: Arizona Geological Survey, 202 pp.

Gibbons, T., 2006, Spatial Arrangement of Deformation Bands and Processes of Formation within Porous Sandstone: Arches National Park, Utah [M.S. thesis]. University of Texas at Austin.
Gillespie, P.A., Howard, C. B., Walsh, J. J., and Watterson, J., 1993, Measurement and characterisation of spatial distributions of fractures: Tectonophysics, v. 226, p. 113-141.
Gomez Torres, L.A., 2007. Characterization of the spatial arrangement of opening-mode fractures [Ph.D. dissertation]. University of Texas at Austin.
Gomez, L.A., and Marrett, R., in review, Spatial arrangement of fractures I — Traditional analyses: Journal of Structural Geology.
Hooker, J.N., Laubach, S.E., and Marrett, R., 2014, A universal power-law scaling exponent for fracture apertures in sandstones: Geological Society of America Bulletin, v. 126, p. 1340-1362.
La Pointe, P.R., and Hudson, J.A., 1985, Characterization and interpretation of rock mass joint patterns: Geological Society of America Special Paper 199, 38 pp.
Laubach, S.E., Reynolds, S.J., Spencer, J.E., and Marshak, S., 1989. Progressive deformation and superposed fabrics related to Cretaceous crustal underthrusting in western Arizona, USA. Journal of Structural Geology 11(6), 735-749.
Laubach, S.E., Vendeville, B.C., and Reynolds, S. J., 1992, Patterns in the development of extensional fault-block shapes from comparison of outcrop-scale faults and experimental physical models, in Larsen, R.M., ed., Structural and Tectonic Modeling and Its Application to Petroleum Geology: Norwegian Petroleum Society Special Publication, p. 95-102.
Marrett, R., and Allmendinger, R.W., 1992, Amount of extension on" small" faults: An example from the Viking graben: Geology, v. 20, p. 47-50.
Marrett, R., Gale, J.F.W., and Gomez, L., in review, Spatial arrangement of fracture arrays III — Correlation analyses: Journal of Structural Geology.
Marrett, R., Ortega, O.J., and Kelsey, C.M., 1999, Extent of power-law scaling for natural fractures in rock: Geology, v. 27, p. 799-802.
Narr, W., and Suppe, J., 1991, Joint spacing in sedimentary rocks: Journal of Structural Geology, v. 13, p. 1037-1048.
Nicol, A., Childs, C., Walsh, J.J., Manzocchi, T., and Schöpfer, M.P.J., 2016, Interactions and growth of faults in an outcrop-scale system: Geological Society, London, Special Publications, v. 439.
Ortega, O.J., Marrett, R.A., and Laubach, S.E., 2006, A scale-independent approach to fracture intensity and average spacing measurement: American Association of Petroleum Geologists Bulletin, v. 90, p. 193-208.
Peacock, D.C.P., and Sanderson, D.J., 1991, Displacements, segment linkage and relay ramps in normal fault zones: Journal of Structural Geology, v. 13, p. 721-733.
Priest, S.D., and Hudson, J.A., 1976, Discontinuity spacings in rock: International Journal of Rock Mechanics and Mining Sciences & Geomechanics Abstracts, v. 13, p. 135-148.

Prior, M.G., Singleton, J.S., and Stockli, D.F., 2016, Late-stage slip history of the Buckskin-Rawhide detachment fault and temporal evolution of the Lincoln Ranch supradetachment basin: new constraints from the middle Miocene Sandtrap conglomerate: Geological Society of America Abstracts with Programs, v. 48.

Reynolds, S.J., Spencer, J.E., Asmerom, Y., DeWitt, E., and Laubach, S.E., 1989, Early Mesozoic uplift in west-central Arizona and southeastern California: Geology, v. 17, p. 207-211.

Reynolds, S.J., Spencer, J.E., Richard, S.M., and Laubach, S.E., 1986, Mesozoic structures in west-central Arizona. Frontiers in geology and ore deposits of Arizona and the Southwest: Arizona Geological Society Digest, v. 16, p. 35-51.

Richard, S.M., Fryxell, J.E., and Sutter, J.F., 1990, Tertiary structure and thermal history of the Harquahala and Buckskin Mountains, west central Arizona: Implications for denudation by a major detachment fault system: Journal of Geophysical Research: Solid Earth, v. 95, p. 19973-19987.

Richard, S.M., Laubach, S.E., Reynolds, S.J., & Spencer, J.E., 1990, Mesozoic thrusting, synplutonic deformation, and Miocene overprinting, Harcuvar complex: a section through the pre-Tertiary crust of west-central Arizona, in Gehrels, G.E., and Spencer, J.E., eds., Geologic excursions through the Sonoran Desert region, Arizona and Sonora: Arizona Geological Survey, Special Paper 7, p. 66-75.

Richard, S.M., Reynolds, S.J., and Spencer, J.E., 1987, Mesozoic stratigraphy of the Little Harquahala Mountains, West-Central Arizona: Arizona Geological Society Digest, v. 18, scale 1:12,800.

Scott, R.J., Foster, D.A., and Lister, G.S., 1998, Tectonic implications of rapid cooling of lower plate rocks from the Buckskin-Rawhide metamorphic core complex, west-central Arizona: Geological Society of America Bulletin, v. 110, p. 588-614.

Scott, R.J., 2004, Geological maps and cross sections of selected areas in the Rawhide and Buckskin Mountains, La Paz and Mohave Counties, Arizona: Arizona Geological Survey Contributed Map, CM-04-D, 10 sheets.

Shackelford, T.J., 1980, Tertiary tectonic denudation of a Mesozoic–early Tertiary(?) gneiss complex, Rawhide Mountains, western Arizona: Geology, v. 8, p. 190-194.

Singleton, J, Bird, E., and Hatfield, M., 2014, Geologic map of the southern Lincoln Ranch basin, Buckskin Mountains, west-central Arizona: Arizona Geological Survey Contributed Map, CM-14-B, scale 1:10,000.

Singleton, J.S., 2015, The transition from large- magnitude extension to distributed dextral faulting in the Buckskin- Rawhide metamorphic core complex, west-central Arizona: Tectonics, v. 34, p. 1685-1708.

Singleton, J.S., Stockli, D.F., Gans, P.B., and Prior, M.G., 2014, Timing, rate, and magnitude of slip on the Buckskin- Rawhide detachment fault, west central Arizona: Tectonics, v. 33, p. 1596-1615.

Singleton, J.S., and Mosher, S., 2012, Mylonitization in the Lower Plate of the Buckskin-Rawhide Detachment Fault, West-Central Arizona: Implications for the Geometric Evolution of Metamorphic Core Complexes: Journal of Structural Geology, v. 39, p. 180-198.

Spencer, J.E., and Reynolds, S.J., 1989, Tertiary structure, stratigraphy, and tectonics of the Buckskin Mountains, in Spencer, J.E., and Reynolds, S.J., eds., Geology and mineral resources of the Buckskin and Rawhide Mountains, west-central Arizona: Arizona Geological Survey Bulletin 198, p. 103-167.

Spencer, J.E., and Reynolds, S.J., 1991, Tectonics of Mid- Tertiary Extension along a transect through west central Arizona: Tectonics, v. 10, p. 1204-1221.

Spencer, J.E., Reynolds, S.J., Anderson, J.L., Davis, G.A., Laubach, S.E., Richard, S.M., and Marshak, S., 1987, Field-trip guide to parts of the Harquahala, Granite Wash, Whipple, and Buckskin Mountains, west-central Arizona and southeastern California, in Davis, G.H., and others, eds., Field-trip guides for Geological Society of America Annual Meeting in Phoenix, Arizona: Arizona Bureau of Geology and Mineral Technology, Geological Survey Branch, Special Paper 5, p. 351-364.

Watterson, J., Walsh, J.J., Gillespie, P.A., and Easton, S., 1996, Scaling systematics of fault sizes on a large-scale range fault map: Journal of Structural Geology, v. 18, p. 199-214.